

Defect Persuade Paramagnetic Properties of Nickel Doped ZnS Nanocrystals and Identification of Structural, Optical, Local Atomic Structure

Soumendra Ghorai

Banaras Hindu University Faculty of Science

Dibyendu Bhattacharyya

Bhabha Atomic Research Centre

Nirmalendu Patra

Bhabha Atomic Research Centre

Shambhu Nath Jha

Bhabha Atomic Research Centre

Anup K Ghosh (✉ akghosh@bhu.ac.in)

Banaras Hindu University <https://orcid.org/0000-0003-3601-8651>

Research Article

Keywords: Nanocrystals, Paramagnetism, X-ray absorption spectroscopy, Photoluminescence

Posted Date: February 19th, 2021

DOI: <https://doi.org/10.21203/rs.3.rs-216850/v1>

License: © ⓘ This work is licensed under a Creative Commons Attribution 4.0 International License.

[Read Full License](#)

Defect persuade paramagnetic properties of nickel doped ZnS nanocrystals and identification of structural, optical, local atomic structure

Soumendra Ghorai^a, Dibyendu Bhattacharyya^b, Nirmalendu Patra^b, Shambhu Nath Jha^b, Anup K. Ghosh^{a,*}

^a*Department of Physics, Institute of Science, Banaras Hindu University, Varanasi-221005, India.*

^b*Atomic & Molecular Physics Division, Bhabha Atomic Research Centre, Mumbai-400085, India.*

*corresponding author: akghosh@bhu.ac.in

Abstract

We have methodically investigated the structural, spectroscopic, local atomic structure and magnetic properties of aquatic $Zn_{1-x}Ni_xS$ ($0 \leq x \leq 0.04$) nanocrystals. The structural study of synthesized samples are observed by X-ray diffraction datas with Rietveld refinement. Proficient decrease of lattice parameters and inter-planar spacing are determined on $Zn_{1-x}Ni_xS$ nanocrystals. The nanocrystalline microstructure is identified by high resolution transmission electron microscopy. The sphalerite morphology of doped samples are observed by scanning electron microscopy. Shrinkage of energy band gap is observed for doped nanocrystals. Defect formation due to doping of Ni ion is observed by photoluminescence spectroscopy with cyan color emission. X-ray absorption spectroscopy is employed for identification of local structures surrounding of Zn and Ni sites of $Zn_{1-x}Ni_xS$ nanocrystals. Extended X-ray absorption fine structure investigation evidenced the existence of nanocluster within the lattice of $Zn_{1-x}Ni_xS$ nanocrystals. X-ray absorption near edge structure studies confirmed incorporation of Ni^{2+} in ZnS lattice of $Zn_{1-x}Ni_xS$ nanocrystals. The single pre-edge feature at Ni K-edge is not relying on concentration of Ni dopant in $Zn_{1-x}Ni_xS$ nanocrystals. The presence of interstitial Ni is identified by significant fraction of Ni-Ni scattering paths on doped samples. $Zn_{1-x}Ni_xS$ nanocrystals exhibit defect persuaded paramagnetism at room temperature.

Key Words: Nanocrystals; Paramagnetism; X-ray absorption spectroscopy; Photoluminescence

1 Introduction

Sulfide doped diluted magnetic semiconductors are important because of their novel potential applications in electronics and optoelectronics [1]. Currently, metal sulfides have attracted more attention in photocatalysis and antimicrobial activities because of their suitable band gap, catalytic function and toxic nature [1]. Zinc sulfide (ZnS) is an important II-VI compound semiconductor which is less toxic in nature and has wide potential applications in nonlinear optical devices, light emitting diodes and solar cells [2]. Doping with transition metal ions as well as rare earth metal ions are renowned pathway to achieve control on the properties of nano scale materials

[2]. Nano-dimensional transition metal doped ZnS is found to exhibit excellent optical and optoelectronic properties that are remarkably different from the bulk [3,4], making it a versatile building block for nanoscale electronic and photonic devices. Nanocrystals with zero dimension have been synthesized by different technique like hydrothermal method [1,3,5,6], wet chemical precipitation method [4,7], micro wave assisted chemical synthesis etc. by transitional metal doped ZnS [8]. Dilute magnetic semiconductors (DMS) having room temperature magnetism which attracted researcher because of the exchange interactions between the spins of the dopant atoms and the carriers on semiconductor host. In this work, nickel (Ni) doped ZnS nanocrystals are synthesized by high temperature aqueous synthesis method. Among the transition metals nickel (Ni) is chosen as the dopant on ZnS nanocrystals because of almost similar ionic radius and substitutes on Zn^{2+} lattice easily. Ni has magnetic moment and theoretical approach of magnetism in nickel based diluted semiconductors reported elsewhere [9-11]. Kumar et al. have shown intrinsic nature of magnetism for Ni doping on ZnS nanoparticles [7]. Saika et al. suggested that ferromagnetism in Ni doped ZnS samples are results of exchange interaction between localized 'd' spins on Ni ions and free delocalized carries [12]. The half metallic ferromagnetism on Ni doped ZnS nanoparticles is reported by Akhtar et al. [13]. Schulz et al. have investigated paramagnetic resonance of Ni doped ZnS crystals [14].

The dependence on atomic number of doped manganese, iron and copper ions, which describe the atomic position of hybridized band energy of transitional metal '3d' shell and '3p' shell of sulfur anti bonding states in $Zn_{1-x}Ni_xS$ (M=Mn, Fe, Co) alloys are reported by Pong et al. [15]. The report of Lawniczak-Jablonska et al. have showed that lower order effect in second nearest shell due to doping of high concentration cation in $Zn_{1-x}Ni_xS$ [16]. They observed only variation in the 'p' state localization but it has limitation for low concentration cation substitution. [16]. In our report, the local electronic structure of $Zn_{1-x}Ni_xS$ surrounding Zn and Ni sites are observed by utilizing synchrotron based X-ray absorption spectroscopy (XAS) which comprise both 'extended X-ray absorption fine structure spectroscopy' (EXAFS) and 'X-ray absorption near edge spectroscopy' (XANES) measurements. The structural information is correlated with X-ray diffraction (XRD) and transmission electron microscopy (TEM) measurements. Scanning electron microscopy demonstrates morphology of nanocrystals. Spectroscopic properties of nanocrystals are observed by 'Ultra-violet visible (UV-visible) spectroscopy' and 'photoluminescence spectroscopy'. Magnetic properties are demonstrated by 'SQUID' ('superconducting quantum interference device magnetometer'). $Zn_{1-x}Ni_xS$ nanocrystals explicated with amalgamation of paramagnetic demeanor and cyan luminescence properties may be utilized for practical device use. In this work the Ni doped ZnS nanocrystals have been prepared by varying the composition of Zn and Ni and we concentrate on the correlation of structural, local atomic structure, spectroscopic and magnetic properties of the samples.

2 Experimental section

2.1 Method of sample preparation

$Zn_{1-x}Ni_xS$ ($0 \leq x \leq 0.04$) nanocrystals (NCs) samples are prepared by modified aqua-synthetic method and labeled as Ni_0 , $Ni_{0.5}$, Ni_1 , Ni_2 and Ni_4 for distinctive Ni dopant on ZnS, $x = 0$, 0.5%, 1%, 2% and 4% receptively. All chemicals were reagent grade and used as obtained. The hydrophilic polymer PVP (polyvinyl pyrrolodine, K-30) was used as a stabilizer to synthesize water-dispersive nanocrystals (NCs). To discuss the whole chemical reaction procedure shortly, four mmol zinc acetate, 6×10^{-3} mmol PVP and appropriate amount (x mmol) of nickel acetate were dissolved in 100 ml distilled water. The solution contained flask was stirred for one hour at room temperature. Afterward, the flask was moved to a hot plate. The temperature of hot plate retained at 473 K. Thereafter, 100 ml solution of sodium sulfide was dripped into the flask under vigorous stirring. In this condition, the reaction was continued to two hours. After that, temperature of the mixed solution was steadily cooled down at laboratory condition. Washing procedure of mixed polymers was carried out by incessant re-dispersion and centrifugation (~ 10000 rotation per minute for 25 minutes). This processes were performed utilizing with distilled water and with ethanol. Thereafter, prepared precipitate were placided and preserved by removing moisture on vacuum oven at 323 K for 14 hours. The white (Ni_0) and slight yellowish ($x=0.005$ to 0.04) powder of Ni doped zinc sulfide NCs were came into possession of grinding the dried precipitate. The exothermic reaction can be expressed as



2.2 Characterizations

The structural parameter of the prepared nanocrystals samples were determined by a Miniflex-600, Rigaku, X-ray diffractometer at room temperature over the range $20^\circ \leq 2\theta \leq 80^\circ$ with increment step size of 0.02° and scanning rate of $2^\circ / \text{minute}$ with CuK_α radiation. Rietveld refinements were performed with ‘Fullproff Suite’ software [17]. The ‘Technai G² Twin field emission transmission electron microscope’ (FEI, Netherland) was utilized to observe the transmission electron microscope (TEM), high resolution TEM (HRTEM) images and selected area electron diffraction (SAED) images and the measurements were performed with fixed current of 10 μA . Scanning electron microscope (SEM) images were taken with ‘EVO Scanning Electron Microscope MA15/18’ (Zeiss, Germany)’ equipped with ‘energy-dispersive X-ray spectroscopy’ (EDS) detector. The micro Raman system ‘LABRAM-HR visible’ (‘Horibra Jobin Yvon’, ‘Model: HR800’) was utilized to observe Raman spectrum. To obsolete structural distortion because of laser warming, the source was adjusted with power head of 10 mW and excited with ~ 633 nm wavelength laser. To obtain ‘Ultra Violet-Visible’ (UV-visible) spectrum the ‘Perkin Elmer Instrument (Lambda-25, USA)’ was utilized with step size of 1 nm [17-18]. The room temperature photoluminescence emission experiments of the prepared samples were performed by utilizing the ‘Perkin Elmer spectro-fluorometer’ (Model: F35). For the

EXAFS experiments of $Zn_{1-x}Ni_xS$ NCs, transmission mode was employed to measure Zn K-edge (9659 eV) and fluorescence mode was employed to measure Ni K-edge (8331 eV). Necessary amount of the synthesized samples were blended accurately with cellulose powder and squeezed to obtain 10 mm (diameter) \times 1 mm (thickness) homogenous circular pellets for obtain proper intensity at K-edges. The pellets were compressed on narrow strip to append with sample holder [17]. The XAS experiments of $Zn_{1-x}Ni_xS$ NCs were performed at ‘Raja Ramanna Centre for Advanced Technology (RRCAT), Indore, India’ at the ‘Energy Scanning EXAFS beam line (BL-9) at Indus-2 Synchrotron with source of 2.5 GeV, 100 mA and with beam size of 0.5 mm \times 0.5 mm at room temperature’ [17,19-22]. A ‘superconducting quantum interference device’ (‘SQUID’; ‘MPMS Quantum Design, Model: 1802’) magnetometer was employed for magnetic experiments. The magnetic field depended (M-H) experiments are performed in the range of ± 2 Tesla (≈ 20000 Oersted) at 300 K. Magnetization as function of temperature (M-T) experiments are performed with fixed magnetizing field of 1000 Oe for Ni_0 and Ni_4 samples within the range of 5 K to 300 K. For M-H and M-T experiments 0.03157 g of Ni_0 sample and 0.02167 g of Ni_1 , Ni_2 and Ni_4 samples are utilized.

3. Results and discussion

3.1 X-ray diffraction

The structural study of the prepared $Zn_{1-x}Ni_xS$ ($0 \leq x \leq 0.04$) nanocrystals (NCs) are investigated by X-ray diffraction (XRD) patterns with the Rietveld refinement and demonstrated in Fig.1. The recorded diffraction peaks of prepared $Zn_{1-x}Ni_xS$ nanocrystals (NCs) are correlative to standard Bragg position of cubic zinc sulfide (Fig.1). The decrease of lattice parameter (Fig.2a) and inter-planar spacing of (111) plane are observed (Fig. 2b) from Rietveld refinement of XRD data. The development of small sized nanocrystals of $Zn_{1-x}Ni_xS$ samples are reason for broadened XRD patterns in comparison to its bulk correlative. It can also be seen that Ni substitution in ZnS lattice does not affect to inclusion or absence of any diffraction peak other than that of pure cubic ZnS manifesting absence of any impurity or secondary phase (i.e. nickel metal, NiS, SO_2) within the range of observed limit of XRD pattern for all prepared samples. However, probability for existence of any impurity peaks or nano cluster without any long range order is discussed in X-ray absorption spectroscopy section. Any significant variation in intensities of the XRD peaks of ZnS due to possible waning of crystallization upon Ni doping has not also been observed in the samples. However, little change in FWHM of main peaks are observed because of Ni ion (0.55 Å) doping, which confirms Ni is entering the lattice of host material [21]. The average crystallite size estimated from the Scherrer’s equation found to be ~ 2.0 nm for all NCs samples [17,22]. In the present set of samples, the microstrain originate because of dislocation which precede to peak broadening. The defect formation mechanism due to Ni dopant in ZnS is identified by photoluminescence studies.

3.2 Scanning electron microscopy

The surface morphology of $Zn_{1-x}Ni_xS$ nanocrystals are verified by SEM images which shown in Fig. 3(a)-3(d). It is observed that agglomerated grains are distributed throughout the surface on $Zn_{1-x}Ni_xS$ nanocrystals. The SEM images relate considerable agglomeration of nanocrystals with sphalerite nanocluster on the surface. The atomic percentages of Ni and ZnS in the respective Ni_0 , Ni_1 , Ni_2 and Ni_4 samples are estimated from the energy dispersive X-ray spectroscopy (EDS) measurements and tabulated in Table 1.

3.3 Transmission electron microscopy

The transmission electron microscopy (TEM) measurements are employed to study microstructure of the prepared nanocrystals (Fig. 4). From the TEM images we observed that allocation of nano-crystallite size of Ni_0 nanocrystals retains within ~ 1.0 nm to ~ 3.20 nm and for higher doped nanocrystals (Ni_4) it retains between ~ 1.1 nm to ~ 3.19 nm. The TEM micrographs demonstrated that nanocrystals are rippleless on surface and tiny spherical in configuration. From the HRTEM images it is observed that interplanar spacing (111) plane of the Ni_0 NCs and the Ni_4 NCs are 0.3088 nm and 0.30704 nm respectively. The existence poly crystalline nature of nanocrystals are evidenced from HRTEM images and ring like SAED patterns.

3.4 Raman spectroscopy

The crystalline quality and the local structural variations on $Zn_{1-x}Ni_xS$ ($0 \leq x \leq 0.04$) nanocrystals are observed with micro-Raman spectroscopy characterization and demonstrated in Fig. 5. The polarization characteristics are identified by Raman spectroscopy with satisfactorily recognized indication of acoustic and optical modes [17,23]. There are two pronounced bands observed at 263 cm^{-1} and 347 cm^{-1} , which are identified as transverse optical (TO) and longitudinal optical (LO) modes, respectively. It is observed that intensity of pronounced modes of doped samples are lower compared to pure nanocrystal sample. It is also identified that the local symmetry of doped nanocrystals are retain similar to the Ni_0 NCs sample. The present observations implied that Ni dopant does not influenced on the lattice structure of nanocrystals and it corroborates with the TEM observations. However, it is observed that the Raman peaks are shifted toward lower energy (Table 2) as compared to the bulk ZnS values [23-26], which signify quantum confinement effects on synthesized Ni_0 NCs and $Zn_{1-x}Ni_xS$ NCs.

3.5 UV-visible spectroscopy

Fig. 6 demonstrated the 'UV-visible absorption' spectrum of the $Zn_{1-x}Ni_xS$ NCs samples. It is observed that an absorption peak located at around 321 nm in Ni_0 NCs sample and also the energy band gap of all samples are estimated from 'Tauc plot' [27]. 'The equation $(\alpha h\nu)^2 = C(h\nu - E_g)$

where, h is Planck's constant, γ is the frequency of radiation, C is a constant and E_g is the energy band gap of the material, is utilized to determine direct energy band of synthesized materials from high absorption region' [27]. The 'Beer-Lambert's relation, $\alpha = 2.303 \times C / t$, where ' t ' is path length of the quartz cuvette and ' C ' is absorbance obtained from UV-visible spectrum, is employed to evaluate the absorption coefficient (α)' [27]. There are number of exciton peaks appearing at different energies corresponding to different sized nanocrystals which overlap with another resulting into broad absorption spectra, so the size distribution is broad [28]. The red shift of absorption wavelength is observed with increase in Ni doping implying that the energy band gap of nanocrystals decreases with increase in doping concentration of $Zn_{1-x}Ni_xS$ NCs. The decrement of band energy gap of synthesized doped nanocrystals arises because of spin exchange interaction with ' sp ' and ' d ' orbital of conduction and valence bands in ZnS and localized ' d ' electrons of Ni ions [28,29]. The shrinkage of energy band gap takes place due to decrement of optical absorption band edge with higher Ni donor density along with excess charge in conduction band and strengthen the interaction potentials between Ni donor electrons and to the host Ni_0 NCs [30].

3.6 X-ray absorption spectroscopy

The quantitative comparison of absorption quality at the Zn K-edge (9659 eV), the normalized 'X-ray absorption near edge structure' (XANES) spectrum of $Zn_{1-x}Ni_xS$ NCs samples including the Zn metal foil and pure ZnS are performed and demonstrated in the Fig. 7.

From Fig. 7, it has been observed that the 1st inflection point at Zn K-edge of $Zn_{1-x}Ni_xS$ samples similar to that of undoped (Ni_0) NCs sample. The result suggests that the oxidation state of Zn atoms retains unperturbed in same state +2 in prepared $Zn_{1-x}Ni_xS$ NCs. The electronic transition from Zn $1s$ state to $4p$ state causes the absorption at Zn K-edge. Moreover, no pre-edge is found out because outer valence ' d ' shell is fully filled. In Fig. 7, a prominent change in white line intensity is observed. The change in unoccupied electron density of states in the outer most orbital may cause such intensity variation [19-21]. From Fig. 7., it has been concluded that the structural symmetry surrounding zinc atoms exhibit similar features for $Zn_{1-x}Ni_xS$ samples. This observation also rules out creation of zinc oxide nanocluster in $Zn_{1-x}Ni_xS$ samples.

The local structure around the absorbing atom is obtained from the quantitative analysis of EXAFS spectra following the standard procedure [19-21]. In order to take care of the oscillations in the absorption spectra $\mu(E)$ has been converted to absorption function $\chi(E)$ defined as follows:

$$\chi(E) = \frac{\mu(E) - \mu_0(E)}{\Delta\mu_0(E_0)} \quad (1)$$

where, absorption edge energy is expressed as E_0 , background of the bare atom expressed as $\mu_0(E_0)$ and $\Delta\mu_0(E_0)$ is expressed as the step in $\mu(E)$ value at the absorption edge. The energy dependent absorption coefficient $\chi(E)$ has been converted to the wave number dependent absorption coefficient $\chi(k)$ using the relation,

$$K = \sqrt{\frac{2m(E - E_0)}{\hbar^2}} \quad (2)$$

where, 'm' is the electron mass. $\chi(k)$ is weighted by k^2 to amplify the oscillation at high k and the $\chi(k)k^2$ functions are fourier transformed to generate the $\chi(R)$ vs. R plots in terms of the real distances from the center of the absorbing atom. The above exercise has been done using the ATHENA subroutine of the Demeter software package [19].

Fig. 8 exhibits the k^2 weighted $\chi(k)$ spectra of the $\text{Zn}_{1-x}\text{Ni}_x\text{S}$ samples while the phase uncorrected fourier transformed $\chi(R)$ vs. R plots obtained from experimental data are exhibited in Fig. 9 where the fourier transform is carried out within a k range of 2-9 \AA^{-1} . The first co-ordination shell exists at a distance of 2.32 \AA which lead to 1st intense peak emerging within the R range of 1.2 \AA to 2.6 \AA distance in the fourier transformed $\chi(R)$ vs. R spectra at the Zn K-edge. Because of higher disorder in 2nd co-ordination shell, no significant peak is observed after 2.5 \AA . Subsequently to extract more quantitative information, the experimentally derived $\chi(R)$ vs. R data are fitted with theoretically simulated plots. For simulation of the theoretical $\chi(R)$ vs. R data pure ZnS structure with lattice parameter ($a = 5.35 \text{\AA}$) determined from 'Rietveld refinement' is utilized and the individual atomic scattering paths are created consequently.

In this structure, the Zn atom placed at (0,0,0) location is circumscribed by four sulfur atoms in the 1st co-ordination shell which created a tetrahedral symmetry with an atomic scattering path of 2.32 \AA and also circumscribed by twelve Zn atoms in adjacent co-ordination sphere at an atomic scattering path of 3.78 \AA . Fig. 8. the best fit $\chi(R)$ vs. R are shown along with the experimental data where fitting has been done in the R range of 1 to 3 \AA . The bond distance (R) of atom to atom and Debye-Waller factor (σ^2) are assorted though the co-ordination number (CN) of each co-ordination shell retained constant during fitting procedure. The ATOMS subroutine of the Demeter software package has been used for the generation of the theoretical EXAFS spectra starting from an assumed crystallographic structure and finally fitting of experimental data with the theoretical spectra has been carried out using the ARTEMIS subroutine.

The fitted results obtained from EXAFS data at the Zn K-edge of $\text{Zn}_{1-x}\text{Ni}_x\text{S}$ samples are tabulated in Table 3. It has been observed that there is no change in 1st co-ordination shell (Zn-S) with

increase in dopant concentration of $\text{Zn}_{1-x}\text{Ni}_x\text{S}$ and it is similar to scattering path (2.28 Å) of Ni_0 sample. So, it has been concluded that lower dopant concentration do not affect the first co-ordination shell of the Zn atoms though their ionic radii are similar ($\text{Zn}^{2+} = 0.60 \text{ \AA}$, $\text{Ni}^{2+} = 0.55 \text{ \AA}$) [19-23].

The quantitative comparison of absorption quality at the Ni K-edge (8331 eV), the normalized X-ray absorption near edge structure (XANES) spectrum of doped NCs samples including the Ni metal foil, standard NiS, and NiSO_4 are performed to obtain oxidation state of nickel ions in $\text{Zn}_{1-x}\text{Ni}_x\text{S}$ samples and demonstrated in Fig. 10. The absorption at Ni-K edge is identical to that observed in Ni doped samples and that of NiS and NiSO_4 , which indicates that on the doped samples Ni ions have +2 oxidation state. Moreover, the absorption spectra of the samples exhibit the presence of single pre-edge feature just below the absorption edge (Fig. 11), which is a typical observation for NiSO_4 sample.

Fig. 12 exhibits k^2 weighted $\chi(k)$ spectra observed at Ni K-edge of the Ni doped ZnS NCs samples. Instead of the Zn atom, Ni atom is placed as central absorbing atom to fit the experimental data at Ni-K edge, assuming the cubic ZnS structure, however, the model is unable to fit the experimental data even at 1st co-ordination shell. In Fig. 13, fourier transformed EXAFS spectra or the $\chi(R)$ vs. R spectra of the 1st co-ordination shell of Ni is shown. To fit experimental data by assuming NiS and NiS_2 structures but such models are unable to fit satisfactorily. Because of the Ni-S bond length is in the range of 2.2 Å so we are unable to fit 1st peak in the $\chi(R)$ vs. R plot of the Ni K-edge data. Thereafter, the experimental data is fitted by assuming standard NiSO_4 (hexahydrate) structure with space group (tP48) where 1st peak of $\chi(R)$ vs. R plot located at ~ 1.5 Å. In this structure Ni atom is circumscribed by 6 O atoms in 1st co-ordination shell and provides information that first intense peak exists within the R range 1-2 Å. Further in the phase uncorrected $\chi(R)$ vs. R spectra, 2nd co-ordination shell (Ni-Ni) arises in the range between 2 to 2.8 Å. The best fit theoretically simulated $\chi(R)$ vs. R plots for the $\text{Zn}_{1-x}\text{Ni}_x\text{S}$ samples assuming the above structure are also shown in Fig. 13 along with the experimental data. The results obtained from EXAFS data at the Ni K-edge of samples are tabulated in Table 4. The Table 4 exhibits that Ni-O bond length acquired from fitting the $\text{Zn}_{1-x}\text{Ni}_x\text{S}$ nanocrystals is ~ 1.99 Å which is close to that in NiSO_4 sample. So it is confirmed that in $\text{Zn}_{1-x}\text{Ni}_x\text{S}$ nanocrystals, Ni atoms create NiSO_4 nanoclusters. It should be noted that the presence of NiSO_4 nanoclusters, however could not be detected by X-ray diffraction, discussed earlier, possibly due to its low concentration and lack of long range order of this phase.

3.7 Photoluminescence spectroscopy

Fig. 14 shows the room temperature photoluminescence (PL) spectrum of the undoped and $Zn_{1-x}Ni_xS$ ($0 \leq x \leq 0.04$) NCs samples excited at wavelength 320 nm. The band-edge emissions of the nanocrystals is observed at about 450 nm which suggests that the trap states emission of ZnS is related to native zinc vacancy [31,32]. The blue band edge emissions at around 460 nm and 472 nm in Ni_0 sample may originate from Zn donor - S acceptor pair which is correlated with the radiative recombination [18]. Such radiative recombination occurs by collision procedure of excitons. Origin of peak at 472 nm is due to sulfur vacancy in the undoped and Ni doped ZnS [18,32]. With increase in doping concentration of Ni dopant on ZnS NCs this peak is decreased because of defect states. A cyan emission peak has been observed in the wavelength region of 484 nm for all $Zn_{1-x}Ni_xS$ NCs samples which is associated with the recombination of free charge carriers and surface defect sites of the nanocrystals.

3.8 Magnetic properties

The field dependent magnetization (M-H) experiments are executed to identify the magnetic characteristics of synthesized samples. The $Zn_{1-x}Ni_xS$ samples exhibit paramagnetic behavior (Fig. 15) in comparison to the diamagnetic Ni_0 NCs which is verified from the magnetic property studies (inset Fig. 15) [32-33]. The paramagnetic nature may be attributed to the surface defects that can exist on the $Zn_{1-x}Ni_xS$ samples. Because of tiny sized of nanocrystals, ratio of surface to volume exceeded considerably, so the surface defect intercede properties have assured signature in the nanomagnetism of $Zn_{1-x}Ni_xS$ samples though the effect of small amount of $NiSO_4$ nanoclusters in the samples, as observed from Ni-K edge XAS measurements cannot be ruled out.

The inextinguishable characteristic of M-H loop is paramagnetic, though the magnetization retained unsaturated till magnetic field of $\sim 2T$ which an indication of little antiferromagnetic interactions in the studied system. The number of Ni ions is higher, hence, Ni-Ni center distance decreases which may enhance antiferromagnetic Ni-Ni interaction at room temperature, that leads to non-saturation of M-H curves of Ni dopant on ZnS.

To find the influence of Ni dopant on ZnS lattice, the thermal variant of magnetization (M-T) with magnetic field of 1000 Oe by following a field cooled protocol is measured for both Ni_0 and Ni_4 NCs samples. The negative magnetization within whole range of temperature studied from M-T curve of the Ni_0 NCs sample (Fig. 16a) suggests that the sample is purely diamagnetic which supports the result of M-H measurement. Moreover, the positive magnetization from M-T curve (Fig. 16b) in whole range of temperature which indicates presence of magnetic interactions in Ni_4 NCs samples. To validate the origin of magnetic ordering, the M-T curve of Ni_4 NCs is analyzed. So we have applied

the standard Curie law, $\frac{M}{H} = \frac{C}{T}$ where C being the Curie constant and T is temperature to the M-T

curve, which resulted a suitable fitting at whole range of observed temperature (Fig.16 b). This result supports that Ni doped ZnS nanocrystals samples exhibit defect induced paramagnetism.

4. Conclusions

The $Zn_{1-x}Ni_xS$ nanocrystals are prepared prosperously by aquatic synthesis route. The Rietveld refinement data obtained from XRD pattern shows decrease of inter-planer spacing due to Ni doping in ZnS lattice, though no major structural change have been observed, which is also correlated with Raman spectroscopy investigations. Scanning electron microscopy shows the spherulite morphology of the samples. A defect induced cyan emission peak observed in the photoluminescence spectra of all Ni doped ZnS. XANES and EXAFS measurements at Ni K-edge confirms that Ni^{2+} ions are incorporated into ZnS lattice and also indicates formation of $NiSO_4$ nanoclusters. The '3d' orbital state with $1s \rightarrow 3d$ transition is responsible for single pre-edge feature on $Zn_{1-x}Ni_xS$ nanocrystals and it has been evidenced that amplitude of such pre-edge is independent of Ni dopant on $Zn_{1-x}Ni_xS$ nanocrystals. The undoped samples are diamagnetic while the doped samples are found to be paramagnetic due to presence of defects or $NiSO_4$ nanoclusters.

Appendix A. Supplementary Materials

Please see supplementary materials for HRTEM images, EDS images, Tauc plots, Inverse susceptibility vs. temperature plot, Refined structural profile parameters of prepared nanocrystals.

Compliance with ethical standards

Conflicts of interest

It has been declared by all authors that there are no conflicts of interests regarding the publication of this article.

Acknowledgements

S.Ghorai thankful to Council of Scientific and Industrial Research (CSIR), Govt. of India for financial support. Dr. Anup K. Ghosh is thankful to DST-FIST program for financial support. We are thankful to Dr. V. Sathe for Raman measurements UGC-DAE, Indore. We are thankful to Prof. D.S. Pandey, Dept. of Chemistry, Institute of Science, BHU for photoluminescence measurements. XRD and HRTEM measurements are carried out at "Central Instrument Facility Centre" (CFIC), IITBHU.

References

- [1] R.S. Kumar, V. Veeravazhuthi, N. Muthukumarasamy, M. Thambidurai, D. Vishnu Shankar, Effect of nickel doping on structural and optical properties of ZnS nanoparticles, *Superlattice Microstruct.* 86 (2015) 552 -558
- [2] M. Dimitrievska, H. Xie, A. J. Jackson, X. Fontane, M. Espindola-Rodriguez, E. Saucedo, A. Perez-Rodriguez, A. Walsh, V. Izquierdo-Roc, Resonant Raman scattering of $\text{ZnS}_x\text{Se}_{1-x}$ solid solutions: the role of S and Se electronic states, *Phys. Chem. Chem. Phys.* 18 (2016) 7632-7640
- [3] V. Ramasamy, K. Praba, G. Murugadoss, Study of optical and thermal properties in nickel doped ZnS nanoparticles using surfactants, *Superlattice Microstruct.* 51 (2012) 699 - 714
- [4] R. Sahrei, S. Darafrin, Preparation of nanocrystalline Ni doped ZnS thin films by ammonia-free chemical bath deposition method and optical properties, *J. Lumin.* 182 (2014) 170-175
- [5] J. Yang, T. Wang, J. Cao, L. Fan, X. Zhang, D. Han, B. Wang, Q. Liu, H. Niu, K. Lin, Facile and shape-controlled growth of the wurtzite ZnS:Ni^{2+} nanoparticles and nanowires, *Superlattice Microstruct.* 71 (2014) 217 -224
- [6] N. Priyadharsini, M. Elango, S. Vairam, M. Thamilselvan, Effect of nickel substitution on structural, optical, magnetic properties and photocatalytic activity of ZnS nanoparticles, *Mat. Sci. Semicon. Proc.* 49 (2016) 68-75
- [7] S. Kumar, C.L. Chen, C.L. Dong, Y.K. Ho, J.F. Lee, T.S. Chan, R. Thangavel, T.K. Chen, B.H. Mok, S.M. Rao, M.K. Wu, Room temperature ferromagnetism in Ni doped ZnS nanoparticles, *J. Alloy. Compd.* 554 (2013) 357-362
- [8] M. Molaei, F. Karimimaskon, A. Lotfiani, M. Samadpour, H. Liu, Synthesis of ZnS:Ni nanocrystals (NCs) using a rapid microwave activated method and investigation of the structural and optical properties, *J. Lumin.* 143 (2013) 649 - 652
- [9] R. Long, N.J. English, Magnetic properties of first-row element-doped ZnS semiconductors: A density functional theory investigation, *Phys. Rev. B* 80 (2009) 115212-115216
- [10] H. Chen, D. Shi, J. Qi, Comparative studies on the magnetic properties of ZnS nanowires doped with transition metal atoms, *J. Appl. Phys.* 109 (2011) 084338-084339
- [11] H.Q. Xie, L. J. Tang, J. L. Tang, P. Peng, Magnetic properties of Ni doped ZnS: First-principles study, *J. Magn. Magn. Mater.* 377 (2015) 239-242
- [12] D.Saika, J. P. Borah, Investigations of doping induced structural, optical and magnetic properties of Ni doped ZnS diluted magnetic semiconductors, *J. Mater. Sci: Mater. Electron.* 28 (2017) 8029-8037

- [13] M.A. Aktar, M.A. Malik, S. Riaz, S. Naseem, Room temperature ferromagnetism and half metallicity in nickel doped ZnS: Experimental and DFT studies, *Mater. Chem. Phys.* 160 (2015) 440-445
- [14] M. Schulz, G.G. Wepfer, Paramagnetic resonance of nickel doped ZnS and CdS crystals, *Solid. State. Commun.* 10 (1972) 405-408
- [15] W.F.P. Pong, R.A. Mayanovic, K.T. Wu, P.K. Tseng, B.A. Bunker, A. Hiraya, M. Watanabe, Influence of transition metal type and content on local order properties of $Zn_{1-x}M_xS$ (M=Mn, Fe, Co) alloys studied using XANES spectroscopy, *Phys. Rev. B* 50(11) (1994) 7371-7377
- [16] K.L. Jablonska, R.J. Iwanowski, Z. Gołacki, A. Traverse, S. Pizzini, A. Fontaine, I. Winter, J. Hormes, Local electronic structure of ZnS and ZnSe doped by Mn, Fe, Co and Ni from X-ray-absorption near edge structure studies, *Phys. Rev. B* 53(3) (1996) 1119-1128
- [17] A. K. Rana, Y. Kumar, P. Rajput, S. N. Jha, D. Bhattacharyya and P. M. Shirage, Search for Origin of Room Temperature Ferromagnetism Properties in Ni doped ZnO Nanostructure, *ACS Appl. Mater. Interfaces* 9(8) (2017) 7691-7700
- [18] A. A. Othman, M. A. Osman, Manar A. Ali, W. S. Mohamed, E. M. M. Ibrahim, Sonochemically synthesized Ni-doped ZnS nanoparticles: structural, optical and photocatalytic properties; *J. Mater. Sci: Mater. Electron.* 31(2020) 1752-1767
- [19] A.K. Poswal, A. Agrawal, A.K. Yadav, C. Nayak, S. Basu, S.R. Kane, C.K. Garg, D. Bhattacharyya, S.N.Jha, N.K. Sahoo, Commissioning and first results of scanning type EXAFS beam line (BL-09) at INDUS-2 synchrotron source, *A.I.P. Conf. Proc.* 1591 (2014) 649-651
- [20] K.M. Hanif, R.W. Meulenberg, G.F. Strouse, Magnetic Ordering in Doped $Cd_{1-x}Co_xSe$ Diluted Magnetic Quantum Dots, *J. Am. Chem. Soc.* 124 (2002) 11495-11502
- [21] S. Basu, C. Nayak, A.K. Yadav, A. Agrawal, A.K. Poswal, D. Bhattacharyya, S.N. Jha, N.K. Sahoo, A comprehensive facility for EXAFS measurements at the INDUS-2 synchrotron source at RRCAT, Indore, India, *J. Phys.: Conf. Ser.* 493 (2014) 012032
- [22] <https://icsd.fiz-karlsruhe.de>
- [23] M. Wu, Z. Wei, W. Zhao, X. Wang, J. Jiang, Optical and magnetic properties of Ni doped ZnS diluted magnetic semiconductors synthesized by hydrothermal method, *J. Nanomater.* 2017 (2017) 1603450
- [24] Z.F. Liu, F.K. Shan, J.Y. Sohn, S.C. Kim, G.Y. Kim, Y.X. Li, Photo luminescence of ZnO: Ga thin films fabricated by pulsed laser deposition technique. *J. Electro ceramics* 13(1-3), 183-187(2004)
- [25] M. Cardona, *Light Scattering in Solids V*, vol. 66, Springer, Berlin, Germany, 1989, pp. 138-140

- [26] W.G. Nilson, Raman spectrum of cubic ZnS, Magnetic Ordering in Doped Cd_{1-x}Co_xSe Diluted Magnetic Quantum Dots, Phys. Rev. 182 (1969) 838
- [27] J.Tauc, Amorphous and Liquid Semiconductors, Plenum, New York, USA, 1974
- [28] S. Sapra, D. D. Sarma, Electronic Structure and Spectroscopy of Semiconductor Nanocrystals, in The Chemistry of Nanomaterials, C.N. Rao, A. Muller, A.K. Cheetham (Eds.), Wiley VCH, Germany, 2, Ch 11, 2004, 375-404
- [29] L. Liu, L. Yang, Y. Pu, D. Xiao, J. Zhu, Optical properties of water-soluble Co²⁺: ZnS semiconductor nanocrystals synthesized by a hydrothermal process. Mater. Lett. 66(1), 121-124 (2012)
- [30] E. Burstein, Anomalous Optical Absorption Limit in InSb, Phys. Rev. 93 (1954) 632-633
- [31] W.S. Ni, Y.J. Lin, C.J. Liu, Y.W. Yang, L. Horng, Luminescence, structural and ferromagnetic properties of Zn_{1-x}Mn_xS_y films for different manganese contents, J. Alloy, Compd 556 (2013) 178-181
- [32] A.K. Shahi, B.K. Pandey, R.K. Swarnkar, R. Gopal, Surfactant assisted surface studies of zinc sulfide nanoparticles, Appl. Surf. Sci. 257 (2011) 9846-9851
- [33] B. Poornaprakash, D. A. Reddy, G. Murali, R.P. Vijayalakshmi, B.K. Reddy, Defect induced paramagnetism in lightly doped ZnS:Fe nanoparticles, Physica E Low Dimens. Syst. Nanostruct. 73 (2015) 63-68
- [34] U. Thibblint, S.R. Micnas, K.A. Chaot, Theory of bound magnetic polarons in diluted magnetic semiconductors, J. Phys. Condens. Matter 1 (1989) 941-956

Table Captions

Table 1. EDS analysis of Zn_{1-x}Ni_xS (0 ≤ x ≤ 0.04) nanocrystals samples

Table 2. Raman peaks of Zn_{1-x}Ni_xS (0 ≤ x ≤ 0.04) nanocrystals and their symmetry assignments

Table 3. The best fitted structural parameters obtained from EXAFS data at Zn K-edge

Table 4. The best fitted structural parameters obtained from EXAFS data at Ni K-edge

Figure Captions

- Fig. 1.** X-ray diffraction data of $\text{Zn}_{1-x}\text{Ni}_x\text{S}$ ($0 \leq x \leq 0.04$) nanocrystals with Rietveld refinement
- Fig. 2.** Change in (a) lattice parameter and (b) (111) inter-planar spacing of $\text{Zn}_{1-x}\text{Ni}_x\text{S}$ ($0 \leq x \leq 0.04$) nanocrystals obtained from Rietveld refinement
- Fig. 3.** The SEM images of (a) Ni_0 , (b) Ni_1 , (c) Ni_2 and (d) Ni_4 nanocrystals (magnification fixed at 60 KX)
- Fig. 4.** (a), (b) and (c) demonstrated low magnification TEM, HRTEM and SAED images of Ni_0 nanocrystals respectively; (d), (e) and (f) showed low magnification TEM, HRTEM and SAED images of Ni_4 nanocrystals respectively
- Fig. 5.** Raman spectrum of the $\text{Zn}_{1-x}\text{Ni}_x\text{S}$ ($0 \leq x \leq 0.04$) NCs observed at room temperature excited with wavelength 632.81 nm
- Fig. 6.** The UV-visible absorption spectrum of $\text{Zn}_{1-x}\text{Ni}_x\text{S}$ ($0 \leq x \leq 0.04$) nanocrystals and inset plot shows change of energy band gap of prepared samples
- Fig. 7.** The normalized XANES data of the $\text{Zn}_{1-x}\text{Ni}_x\text{S}$ ($0 \leq x \leq 0.04$) nanocrystals observed at Zn K-edge
- Fig. 8.** The k^2 weighted $\chi(k)$ spectra obtained at Zn K-edge of the $\text{Zn}_{1-x}\text{Ni}_x\text{S}$ ($0 \leq x \leq 0.04$) nanocrystals
- Fig. 9.** The best fitted experimental $\chi(R)$ vs. R data with theoretically created plot (showed in solid line) at Zn K-edge of (a) Ni_0 , (b) $\text{Ni}_{0.5}$, (c) Ni_1 , (d) Ni_2 and (e) Ni_4 nanocrystals
- Fig. 10.** The normalized XANES data observed at Ni K-edge of the $\text{Zn}_{1-x}\text{Ni}_x\text{S}$ nanocrystals
- Fig. 11.** The pre-edge characteristic of the nickel doped ZnS NCs with reference to NiS and NiSO_4 samples at Ni K-edge
- Fig. 12.** The k^2 weighted $\chi(k)$ spectra obtained at Ni K-edge of the $\text{Zn}_{1-x}\text{Ni}_x\text{S}$ nanocrystals
- Fig. 13.** The best fitted experimental $\chi(R)$ vs. R data with theoretically created data (showed in solid line) at Ni K-edge of the $\text{Zn}_{1-x}\text{Ni}_x\text{S}$ nanocrystals
- Fig. 14.** The photoluminescence spectrum of $\text{Zn}_{1-x}\text{Ni}_x\text{S}$ ($0 \leq x \leq 0.04$) nanocrystals observed by exciting at 320 nm
- Fig. 15.** Magnetization vs. applied field measured in the range of ± 20000 Oe at 300 K of Ni_1 , Ni_2 , nanocrystals samples and the inset is the magnetization of Ni_0 nanocrystals observed in the range of ± 70000 Oe at 300 K
- Fig. 16.** Magnetization vs. temperature plot of (a) Ni_0 nanocrystals and (b) Ni_4 nanocrystals (with fitting) at fixed field of 1000 Oe

Tables

Table 1. EDS analysis of $Zn_{1-x}Ni_xS$ ($0 \leq x \leq 0.04$) nanocrystals samples

Sample	Zinc Sulfide	Nickel
Ni ₀	100	0
Ni ₁	99.03 (± 0.01)	0.97 (± 0.01)
Ni ₂	98.08 (± 0.03)	1.92 (± 0.03)
Ni ₄	96.07 (± 0.02)	3.93 (± 0.02)

Table 2. Raman peaks of $Zn_{1-x}Ni_xS$ ($0 \leq x \leq 0.04$) nanocrystals and their symmetry assignments

Vibration frequency (cm ⁻¹)					
Ni ₀	Ni ₁	Ni ₂	Ni ₄	Assignments	Process
263	263	266	267	Transverse optical mode	1 st Order
347	348	349	349	Longitudinal optical mode	1 st Order

Table 3. The best fitted structural parameters obtained from EXAFS data at Zn K-edge

Sample	Scattering paths Zn – S × 4		
	R (Å)	σ^2 (Å ²)	R_{factor}
Ni₀	2.26 ± 0.01	0.008 ± 0.005	0.008
Ni_{0.5}	2.26 ± 0.01	0.005 ± 0.002	0.006
Ni₁	2.28 ± 0.01	0.006 ± 0.002	0.006
Ni₂	2.28 ± 0.01	0.002 ± 0.002	0.004
Ni₄	2.28 ± 0.01	0.002 ± 0.002	0.005

Table 4. The best fitted structural parameters obtained from EXAFS data at Ni K-edge

Scattering paths	Parameters	NiSO ₄	Ni _{0.5}	Ni ₁	Ni ₂	Ni ₄
Ni – O × 6	R (Å)	2.03 ± 0.01	2.04 ± 0.01	2.04 ± 0.02	2.03 ± 0.02	2.01 ± 0.01
	σ^2 (Å ²)	0.006 ± 0.001	0.006 ± 0.001	0.006 ± 0.001	0.007 ± 0.002	0.005 ± 0.002
Ni – Ni × 2	R (Å)	3.30 ± 0.03	3.09 ± 0.02	3.09 ± 0.02	3.04 ± 0.05	2.95 ± 0.05
	σ^2 (Å ²)	0.029 ± 0.009	0.006 ± 0.002	0.010 ± 0.006	0.004 ± 0.003	0.012 ± 0.010
	R_{factor}	0.002	0.006	0.007	0.023	0.022

Figures

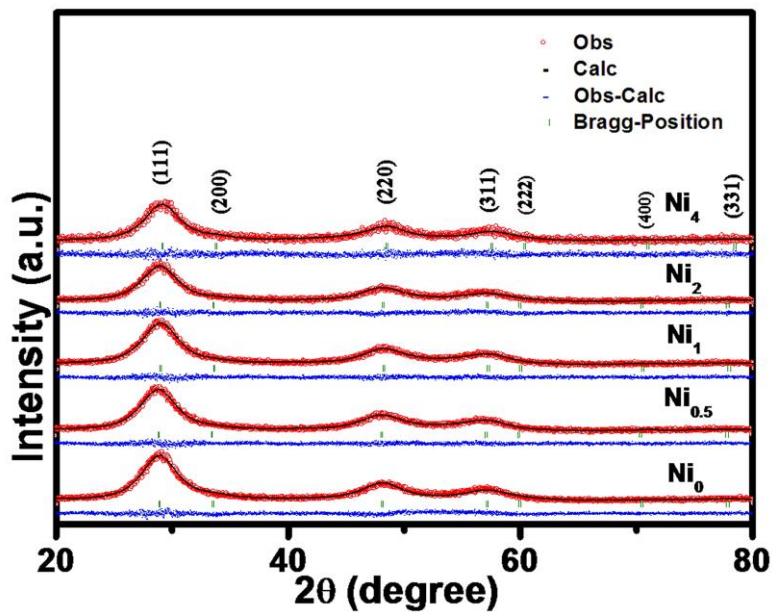


Fig. 1. X-ray diffraction data of $Zn_{1-x}Ni_xS$ ($0 \leq x \leq 0.04$) nanocrystals with Rietveld refinement

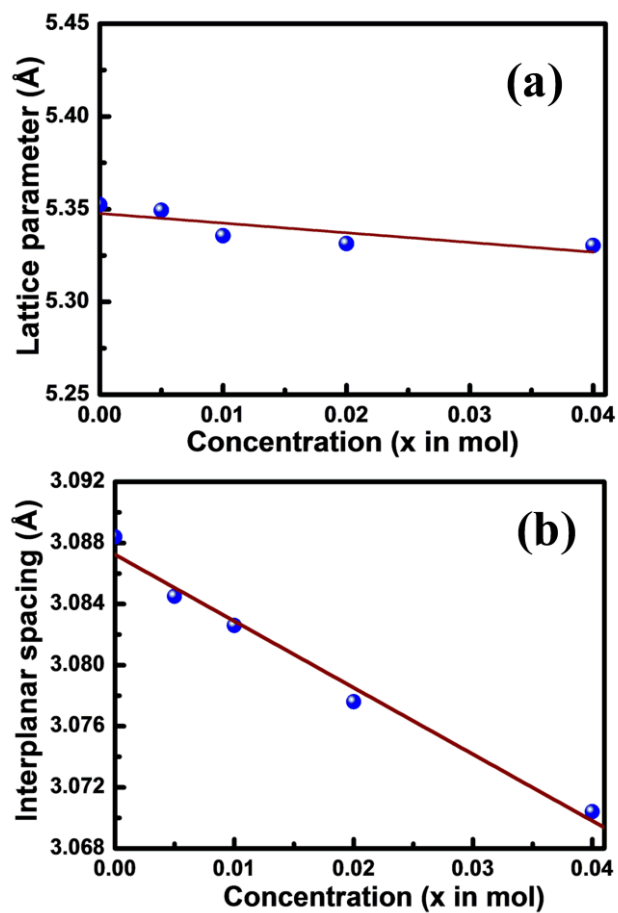


Fig. 2. Change in (a) lattice parameter and (b) (111) inter-planar spacing of $Zn_{1-x}Ni_xS$ ($0 \leq x \leq 0.04$) nanocrystals obtained from Rietveld refinement

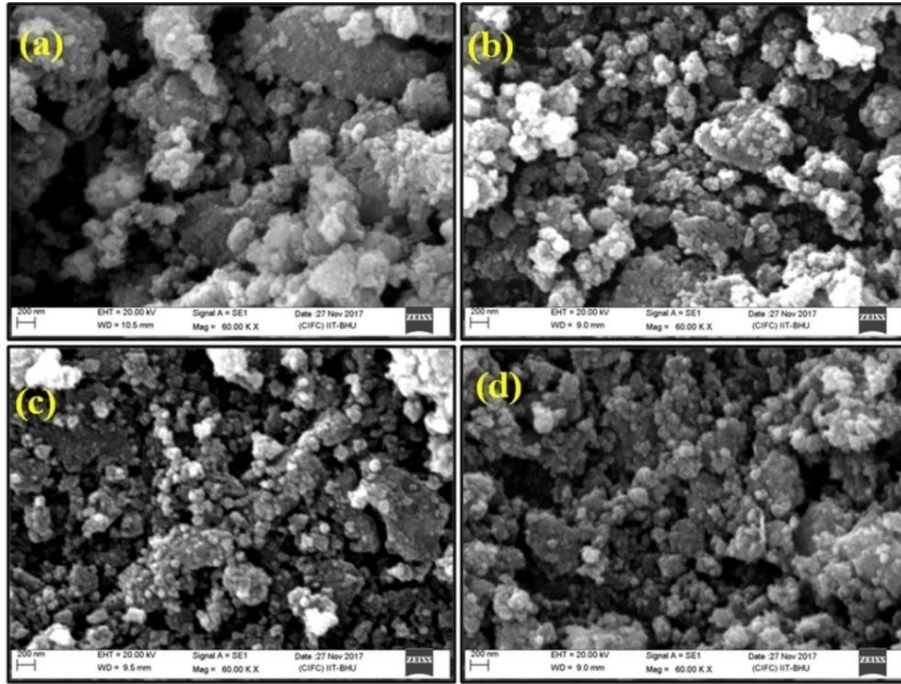


Fig. 3. The SEM images of (a) Ni₀, (b) Ni₁, (c) Ni₂ and (d) Ni₄ nanocrystals (magnification fixed at 60 KX)

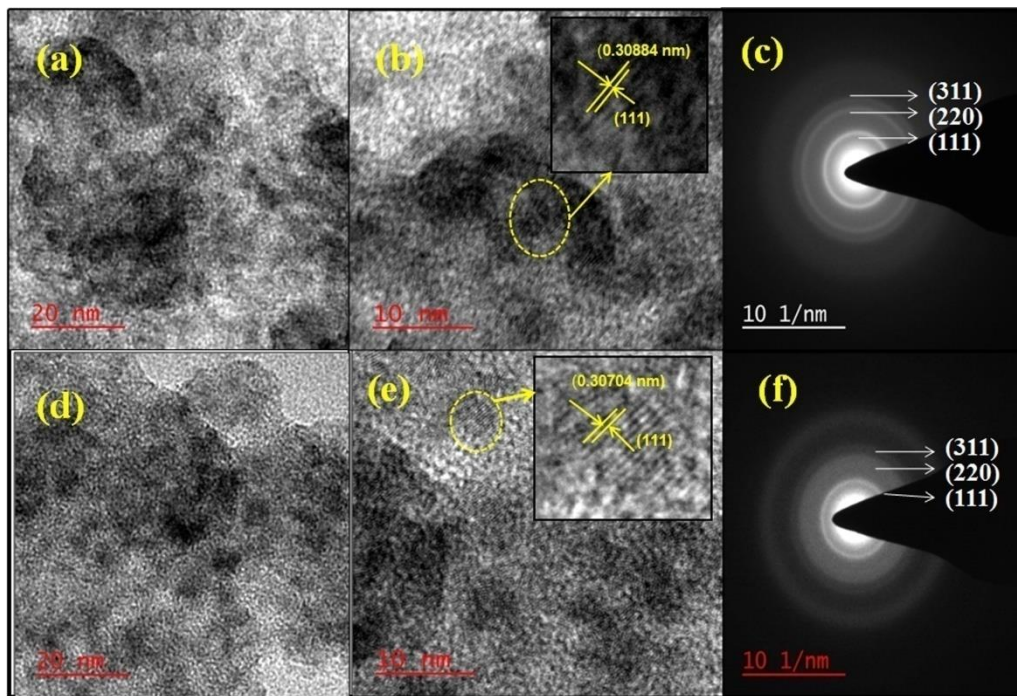


Fig. 4. (a), (b) and (c) demonstrated low magnification TEM, HRTEM and SAED images of NiO nanocrystals respectively; (d), (e) and (f) showed low magnification TEM, HRTEM and SAED images of Ni_4 nanocrystals respectively

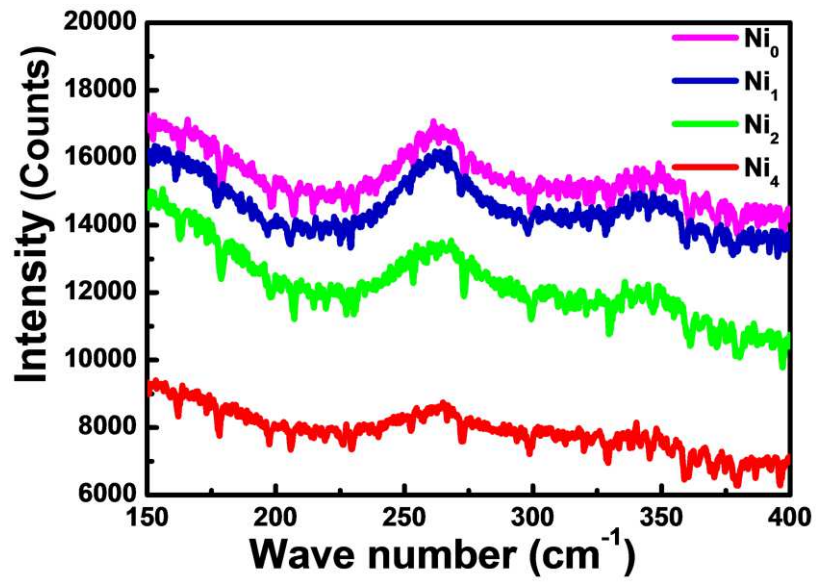


Fig. 5. Raman spectrum of the $\text{Zn}_{1-x}\text{Ni}_x\text{S}$ ($0 \leq x \leq 0.04$) NCs observed at room temperature excited with wavelength 632.81 nm

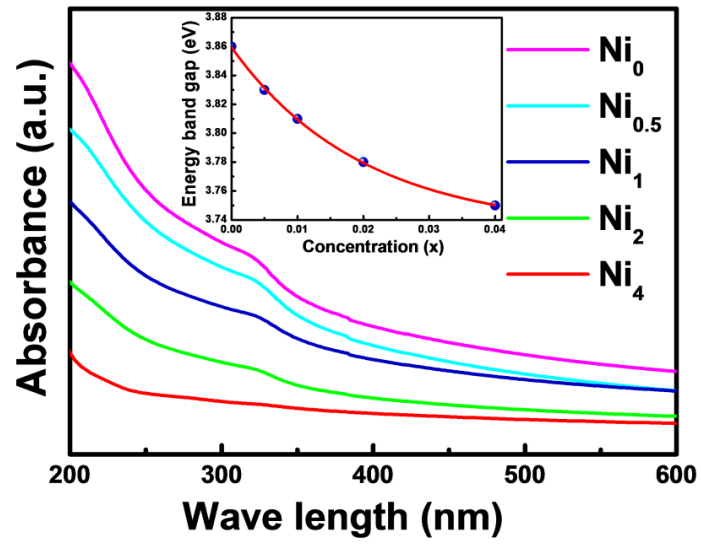


Fig. 6. The UV-visible absorption spectrum of Zn_{1-x}Ni_xS (0 ≤ x ≤ 0.04) nanocrystals and inset plot shows change of energy band gap of prepared samples

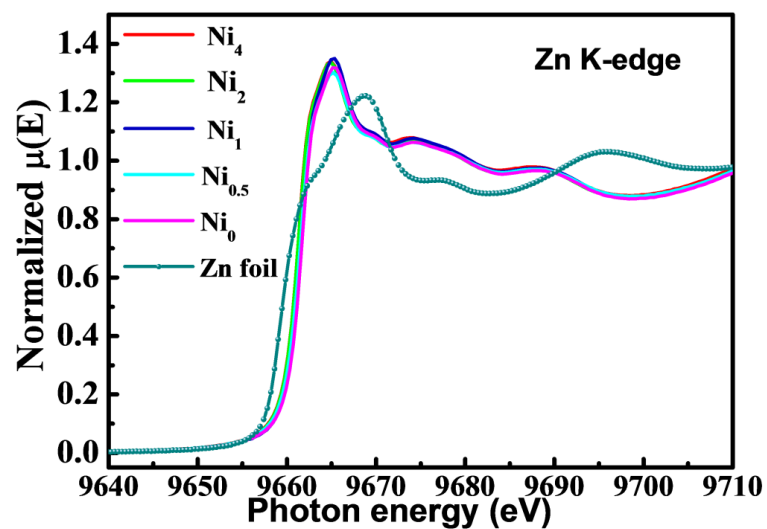


Fig. 7. The normalized XANES data of the $Zn_{1-x}Ni_xS$ ($0 \leq x \leq 0.04$) nanocrystals observed at Zn K-edge

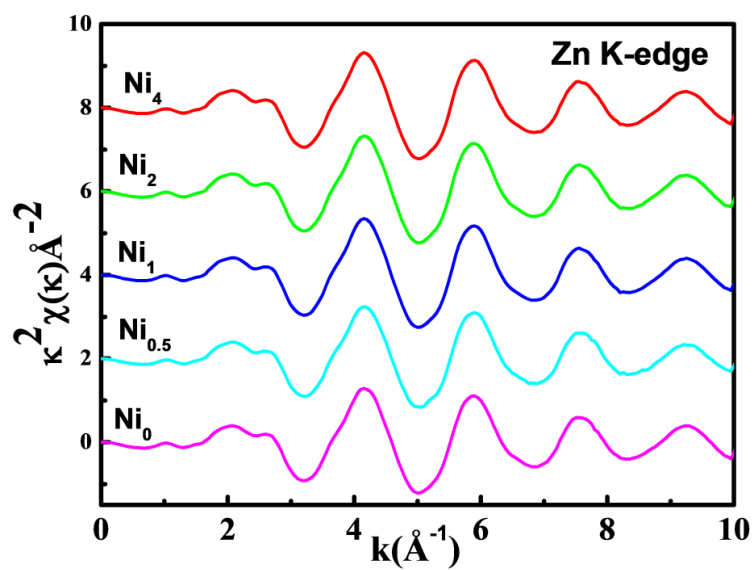


Fig. 8. The k^2 weighted $\chi(k)$ spectra obtained at Zn K-edge of the $\text{Zn}_{1-x}\text{Ni}_x\text{S}$ ($0 \leq x \leq 0.04$) nanocrystals

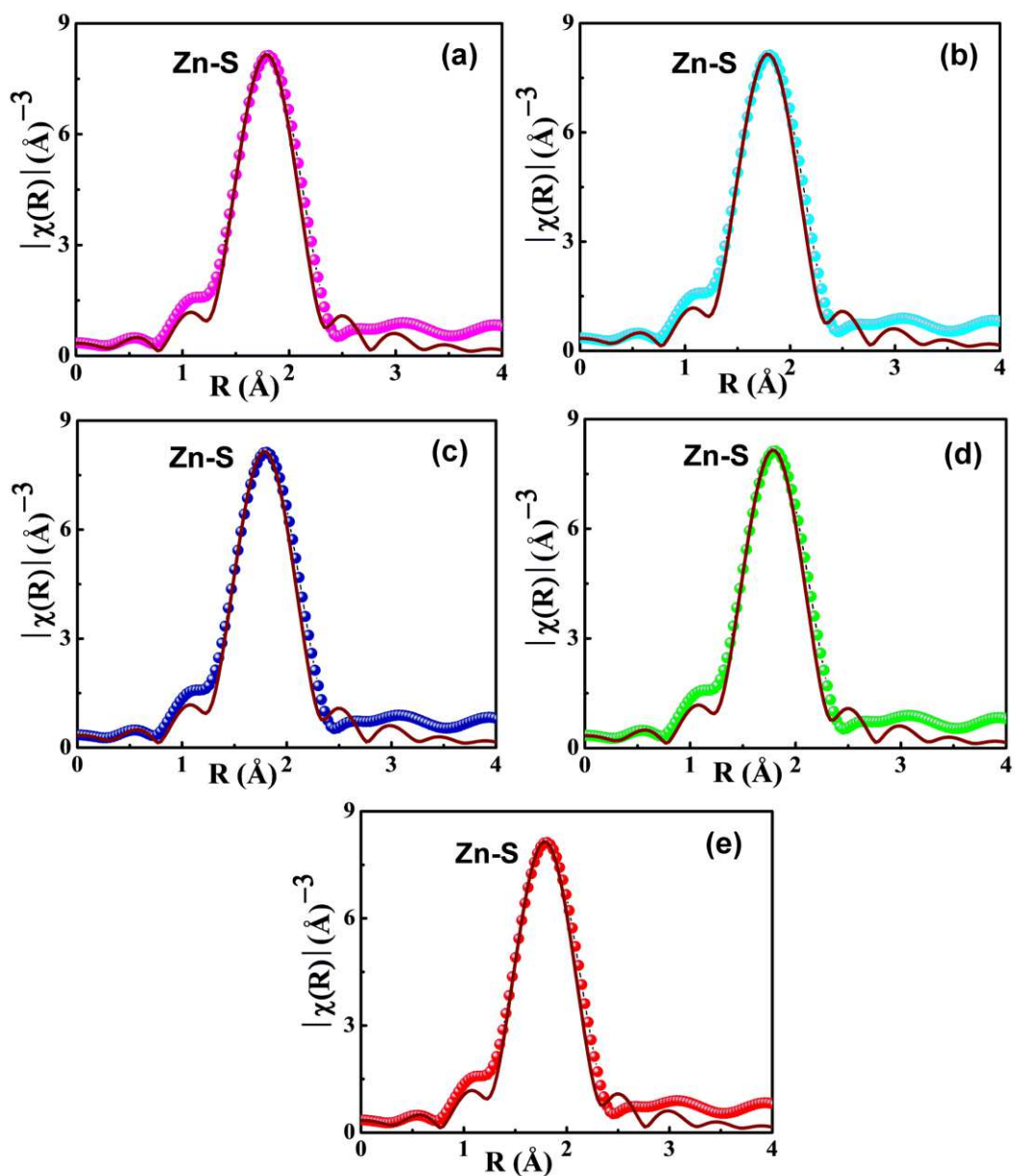


Fig. 9. The best fitted experimental $\chi(R)$ vs. R data with theoretically created plot (showed in solid line) at Zn K-edge of (a) Ni_0 , (b) $\text{Ni}_{0.5}$, (c) Ni_1 , (d) Ni_2 and (e) Ni_4 nanocrystals

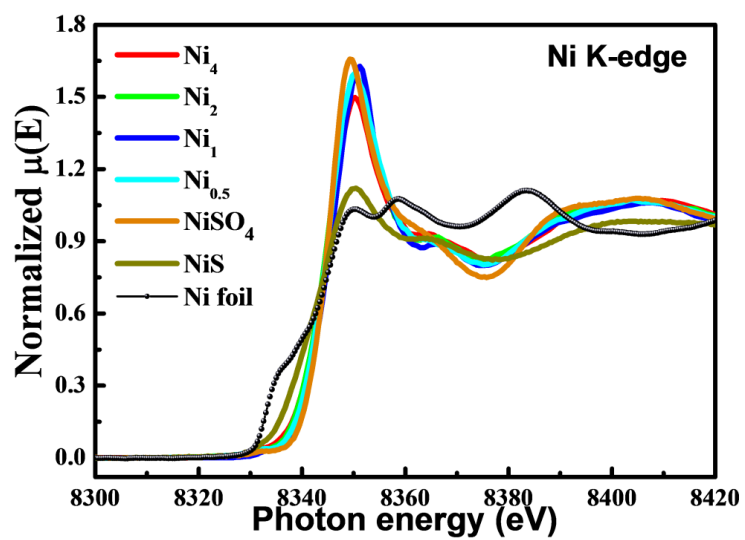


Fig. 10. The normalized XANES data observed at Ni K-edge of the $\text{Zn}_{1-x}\text{Ni}_x\text{S}$ nanocrystals

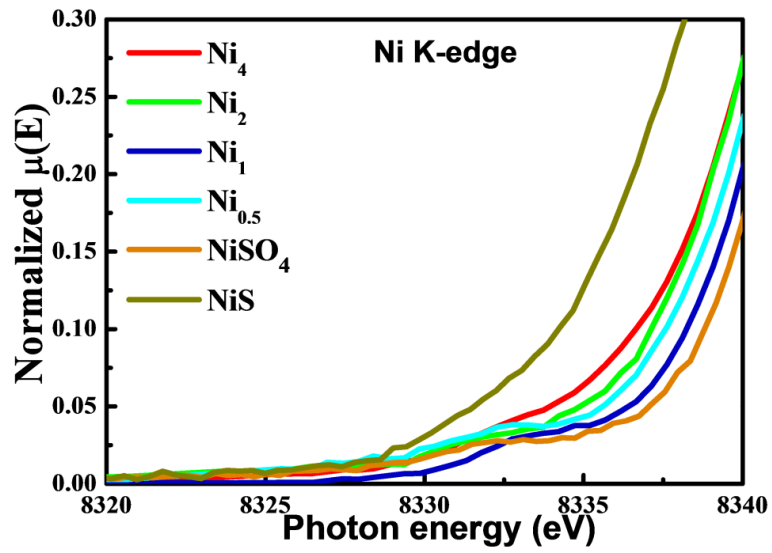


Fig. 11. The pre-edge characteristic of the nickel doped ZnS NCs with reference to NiS and $NiSO_4$ samples at Ni K-edge

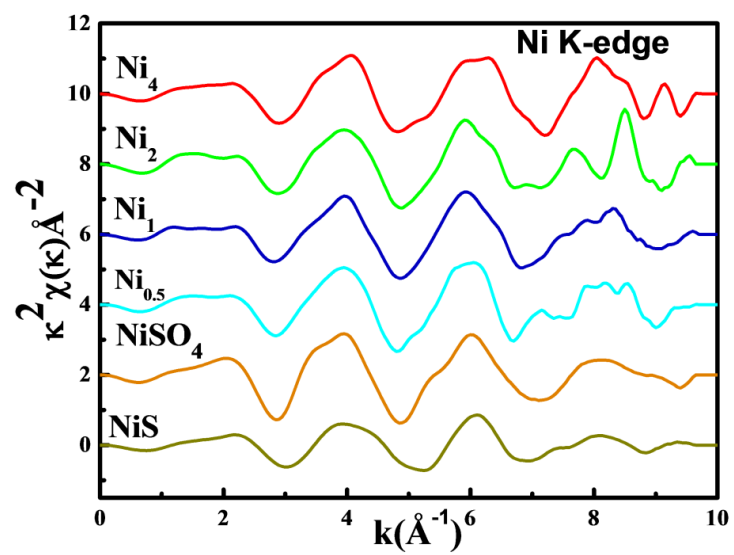


Fig. 12. The k^2 weighted $\chi(k)$ spectra obtained at Ni K-edge of the $\text{Zn}_{1-x}\text{Ni}_x\text{S}$ nanocrystals

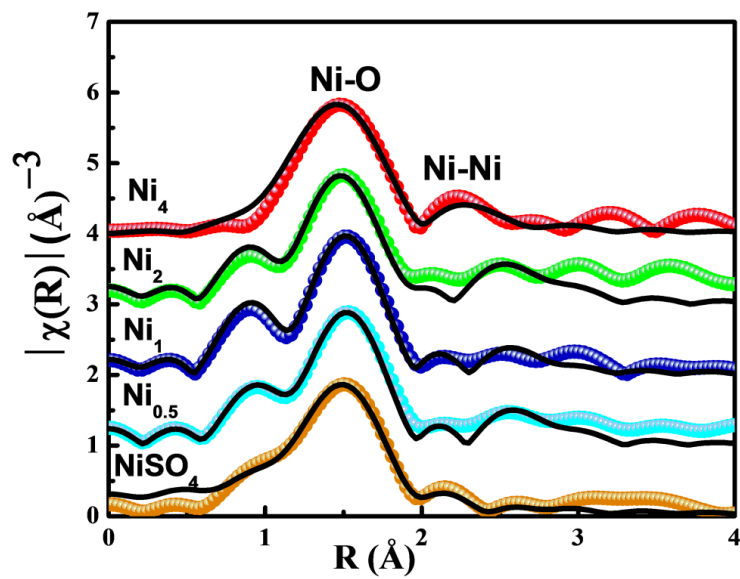


Fig. 13. The best fitted experimental $\chi(R)$ vs. R data with theoretically created data (showed in solid line) at Ni K-edge of the $\text{Zn}_{1-x}\text{Ni}_x\text{S}$ nanocrystals

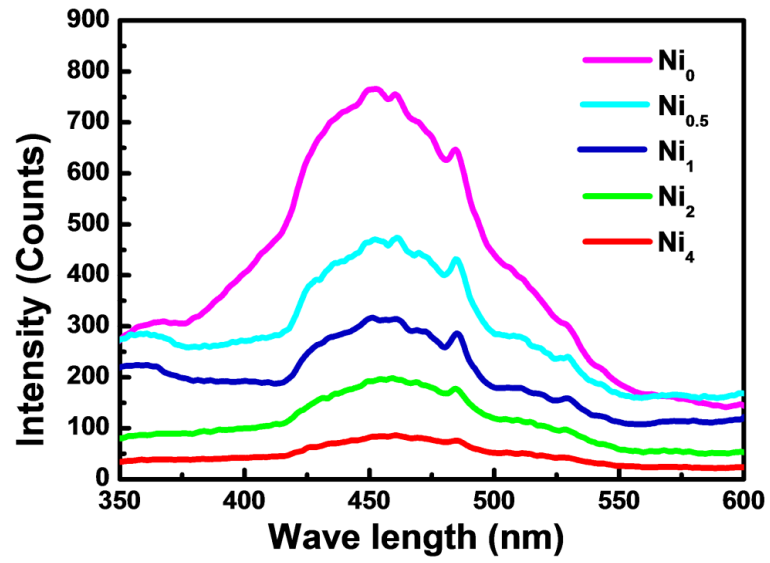


Fig. 14. The photoluminescence spectrum of $Zn_{1-x}Ni_xS$ ($0 \leq x \leq 0.04$) nanocrystals observed by exciting at 320 nm

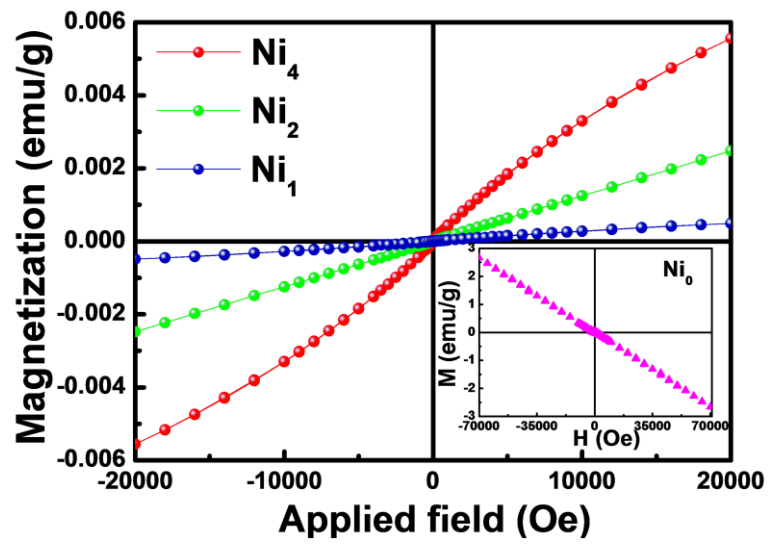


Fig. 15. Magnetization vs. applied field measured in the range of ± 20000 Oe at 300 K of Ni_1 , Ni_2 , Ni_4 nanocrystals samples and the inset is the magnetization of Ni_0 nanocrystals observed in the range of ± 70000 Oe at 300 K

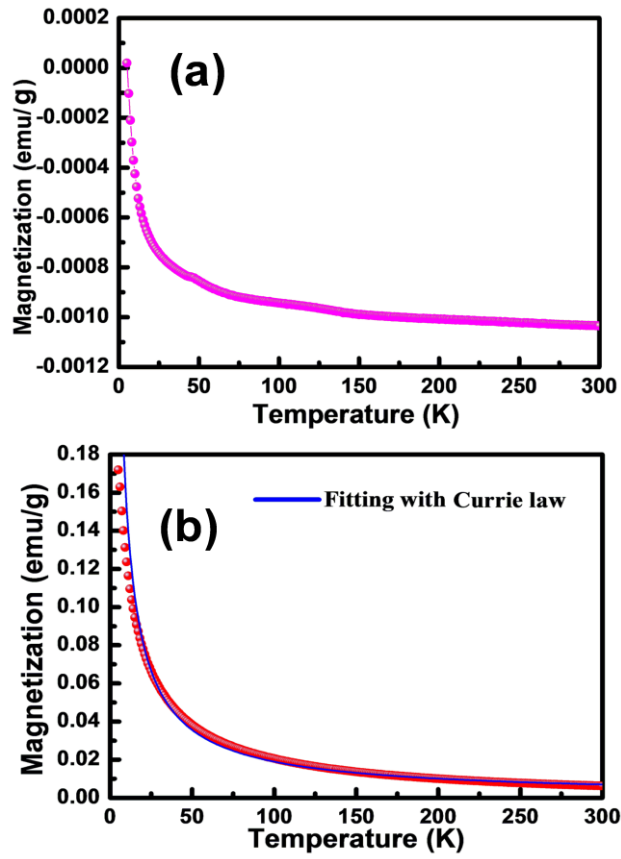


Fig. 16. Magnetization vs. temperature plot of (a) Ni_0 nanocrystals and (b) Ni_4 nanocrystals (with fitting) at fixed field of 1000 Oe

Figures

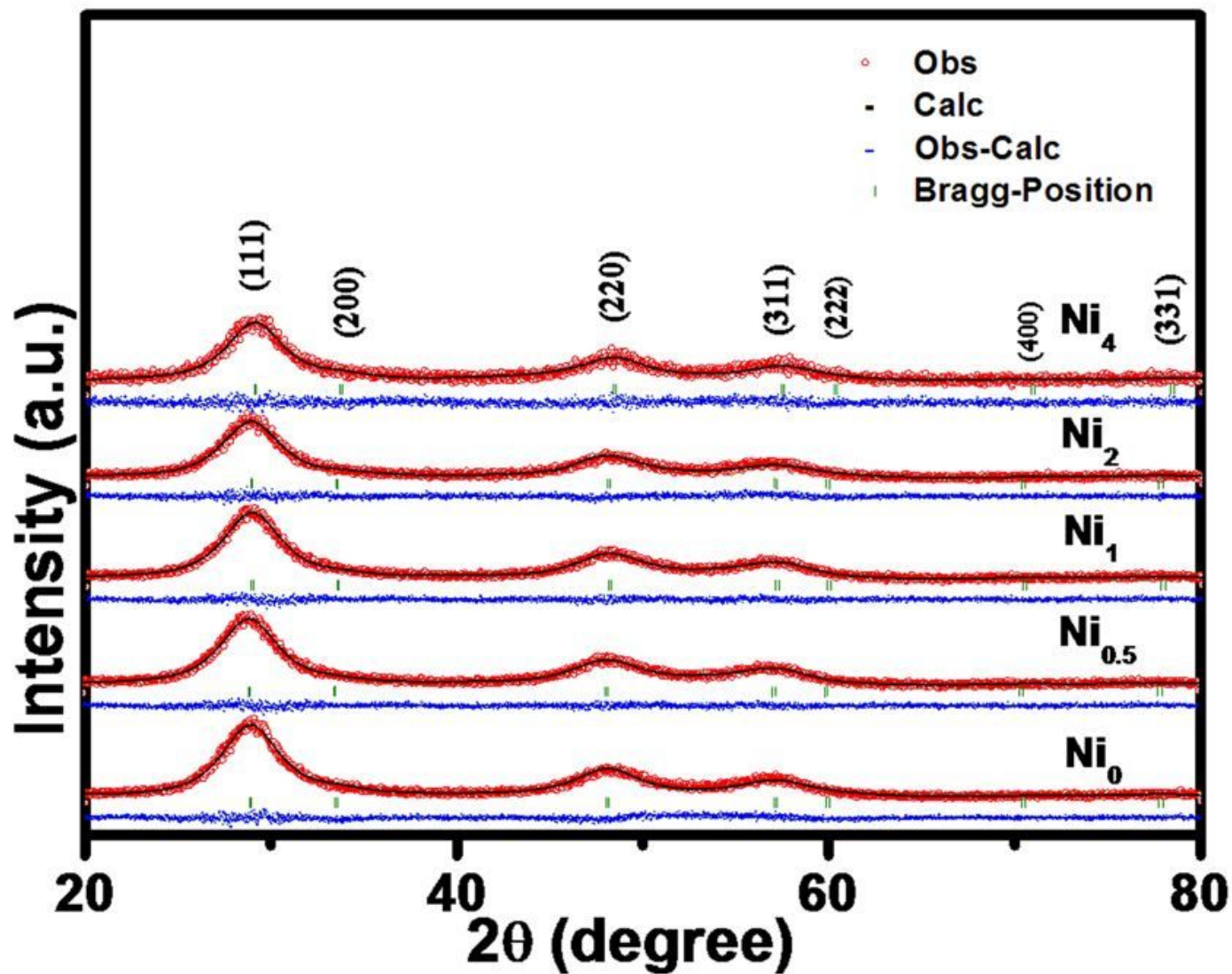


Figure 1

X-ray diffraction data of Zn_{1-x}Ni_xS ($0 \leq x \leq 0.04$) nanocrystals with Rietveld refinement

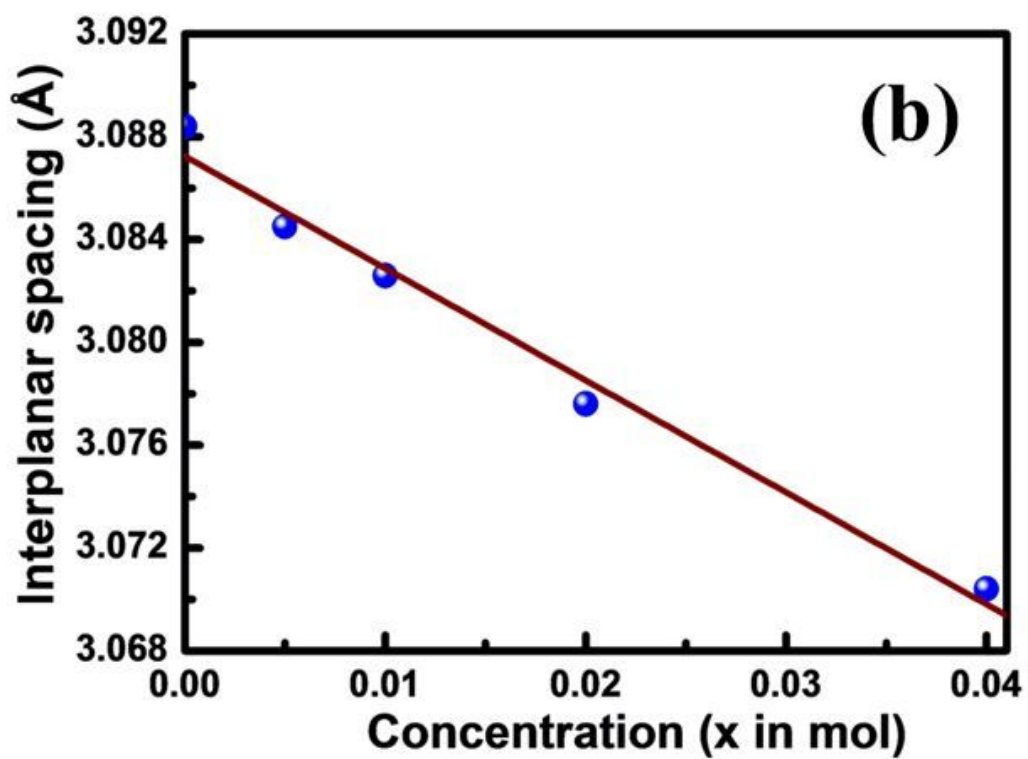
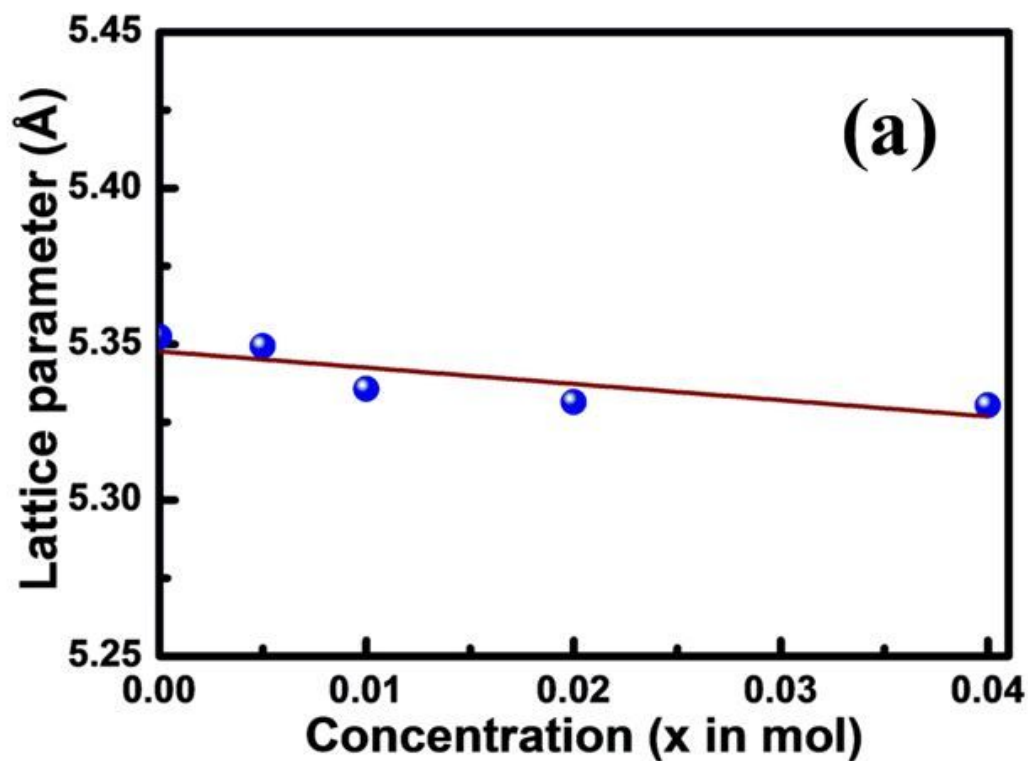


Figure 2

Change in (a) lattice parameter and (b) (111) inter-planar spacing of $Zn_{1-x}Ni_xS$ ($0 \leq x \leq 0.04$) nanocrystals obtained from Rietveld refinement

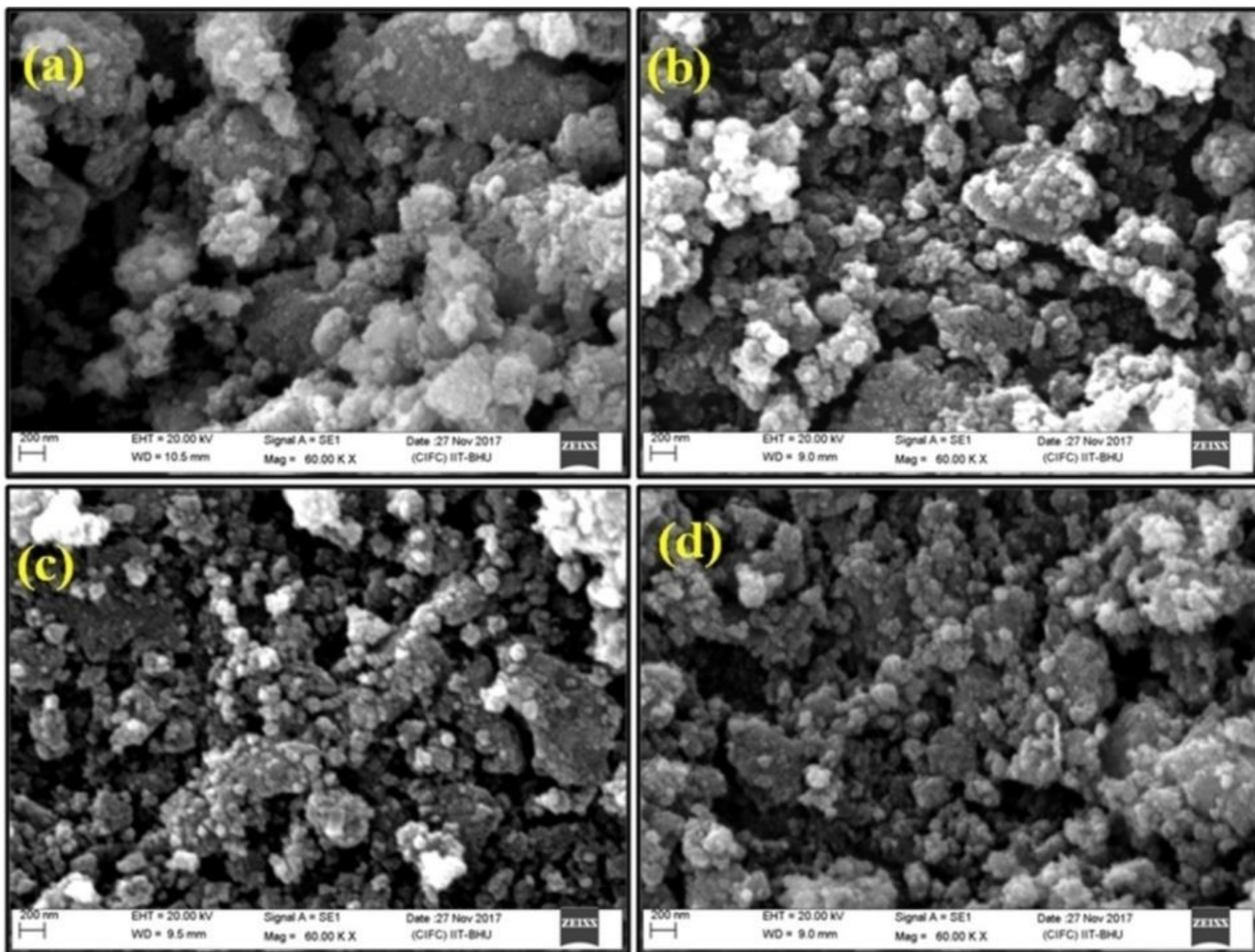


Figure 3

The SEM images of (a) Ni0, (b) Ni1, (c) Ni2 and (d) Ni4 nanocrystals (magnification fixed at 60 KX)

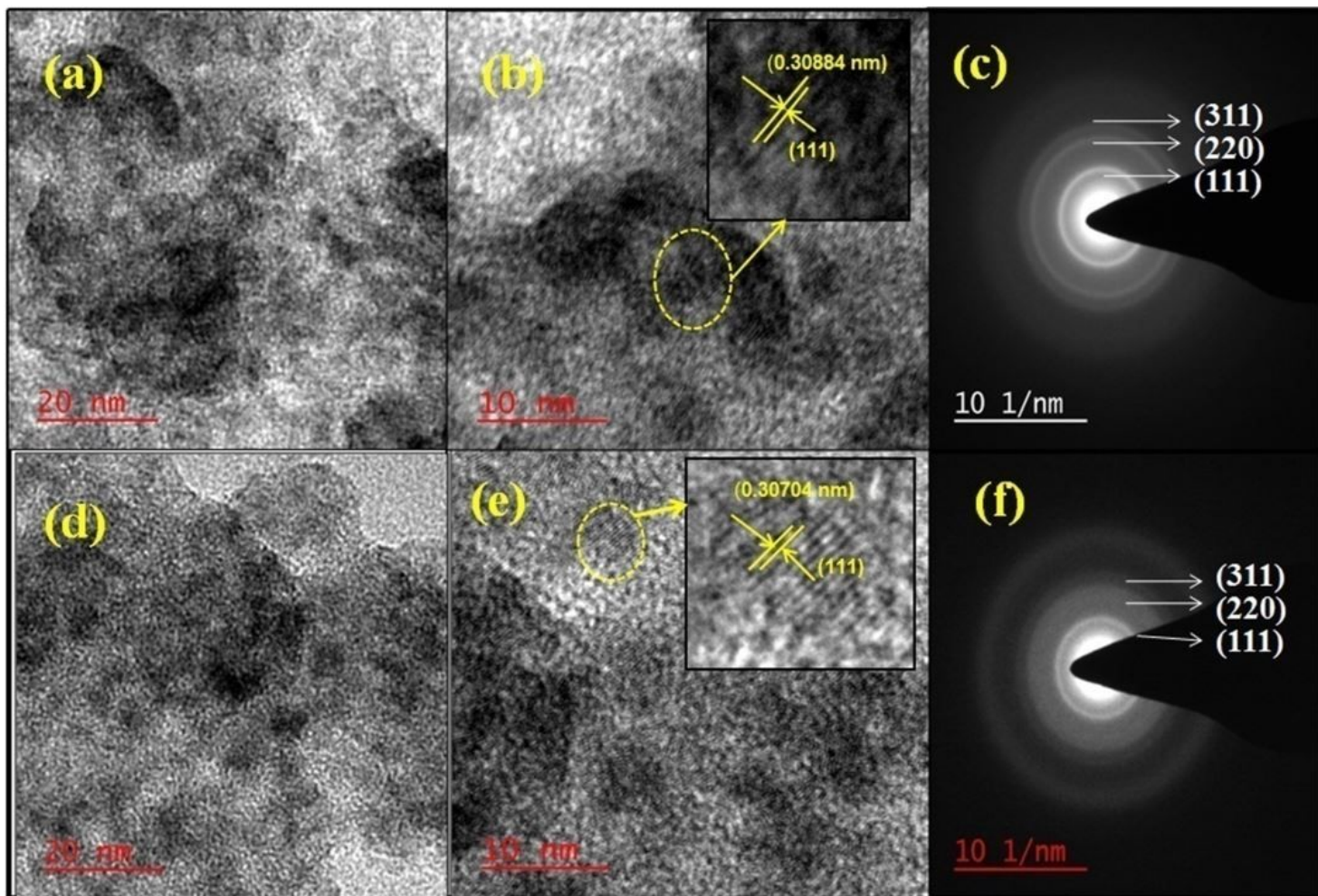


Figure 4

(a), (b) and (c) demonstrated low magnification TEM, HRTEM and SAED images of Ni₀ nanocrystals respectively; (d), (e) and (f) showed low magnification TEM, HRTEM and SAED images of Ni₄ nanocrystals respectively

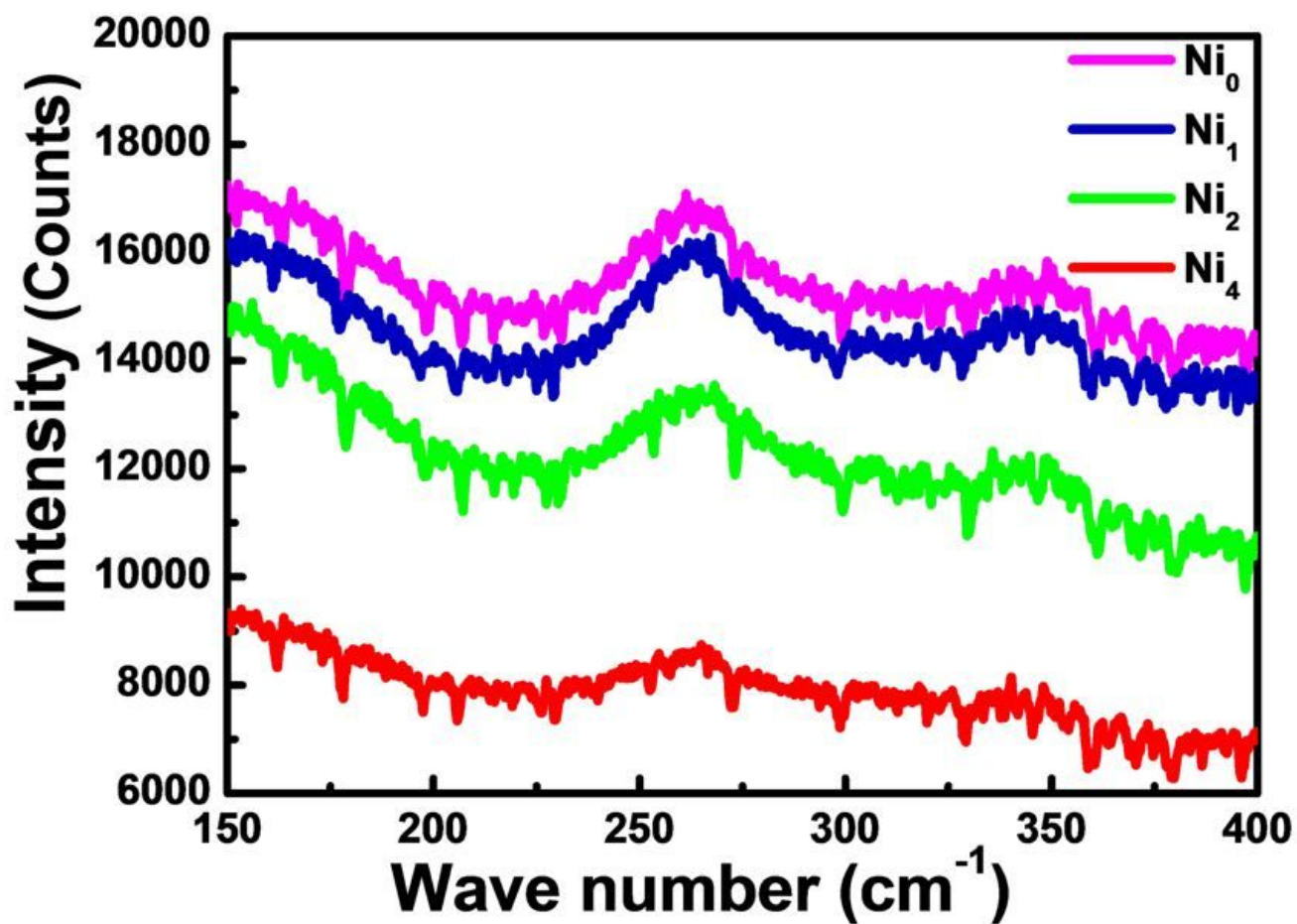


Figure 5

Raman spectrum of the Zn_{1-x}Ni_xS ($0 \leq x \leq 0.04$) NCs observed at room temperature excited with wavelength 632.81 nm

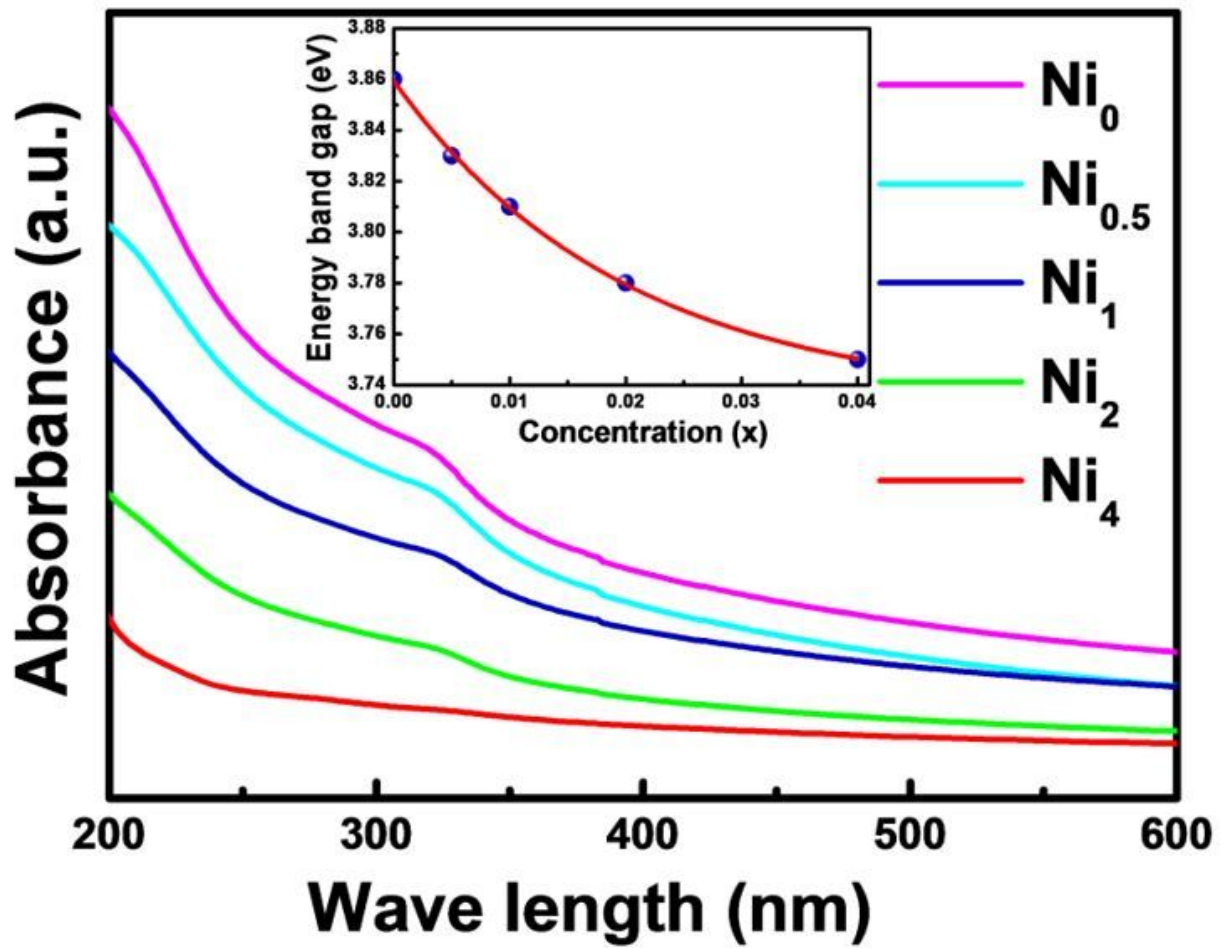


Figure 6

The UV-visible absorption spectrum of Zn_{1-x}Ni_xS ($0 \leq x \leq 0.04$) nanocrystals and inset plot shows change of energy band gap of prepared samples

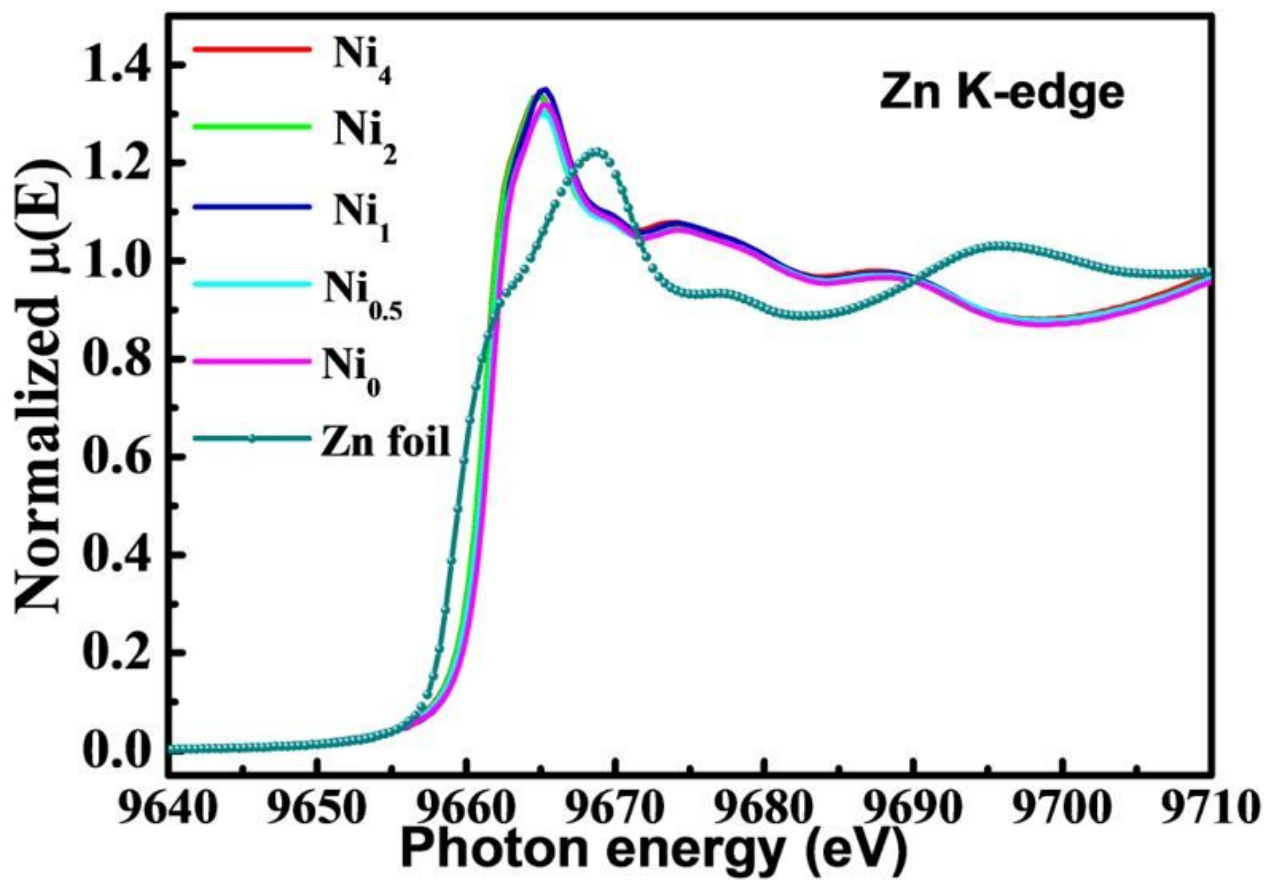


Figure 7

The normalized XANES data of the $Zn_{1-x}Ni_xS$ ($0 \leq x \leq 0.04$) nanocrystals observed at Zn K-edge

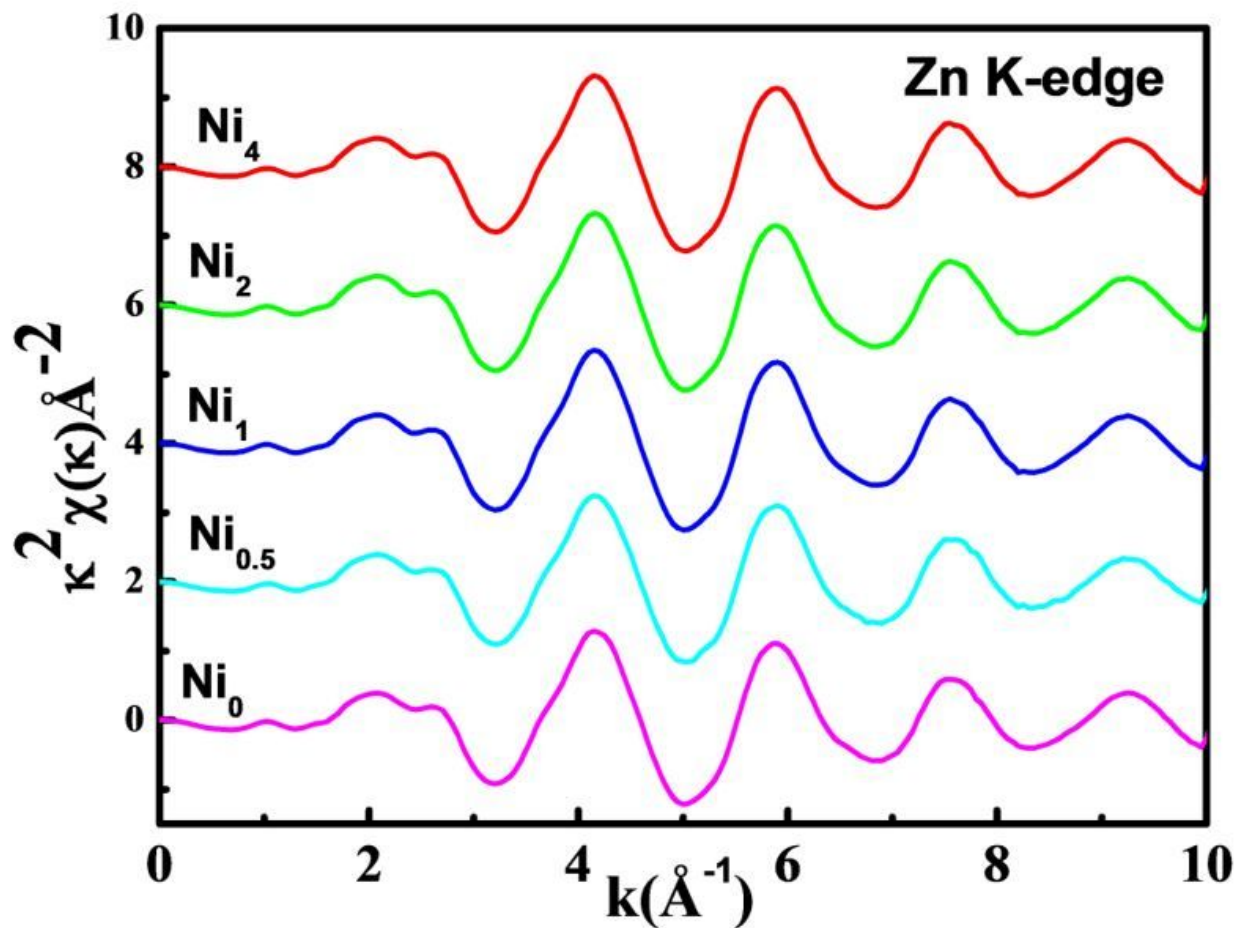


Figure 8

The K2 weighted $\chi(k)$ spectra obtained at Zn K-edge of the Zn_{1-x}Ni_xS ($0 \leq x \leq 0.04$) nanocrystals

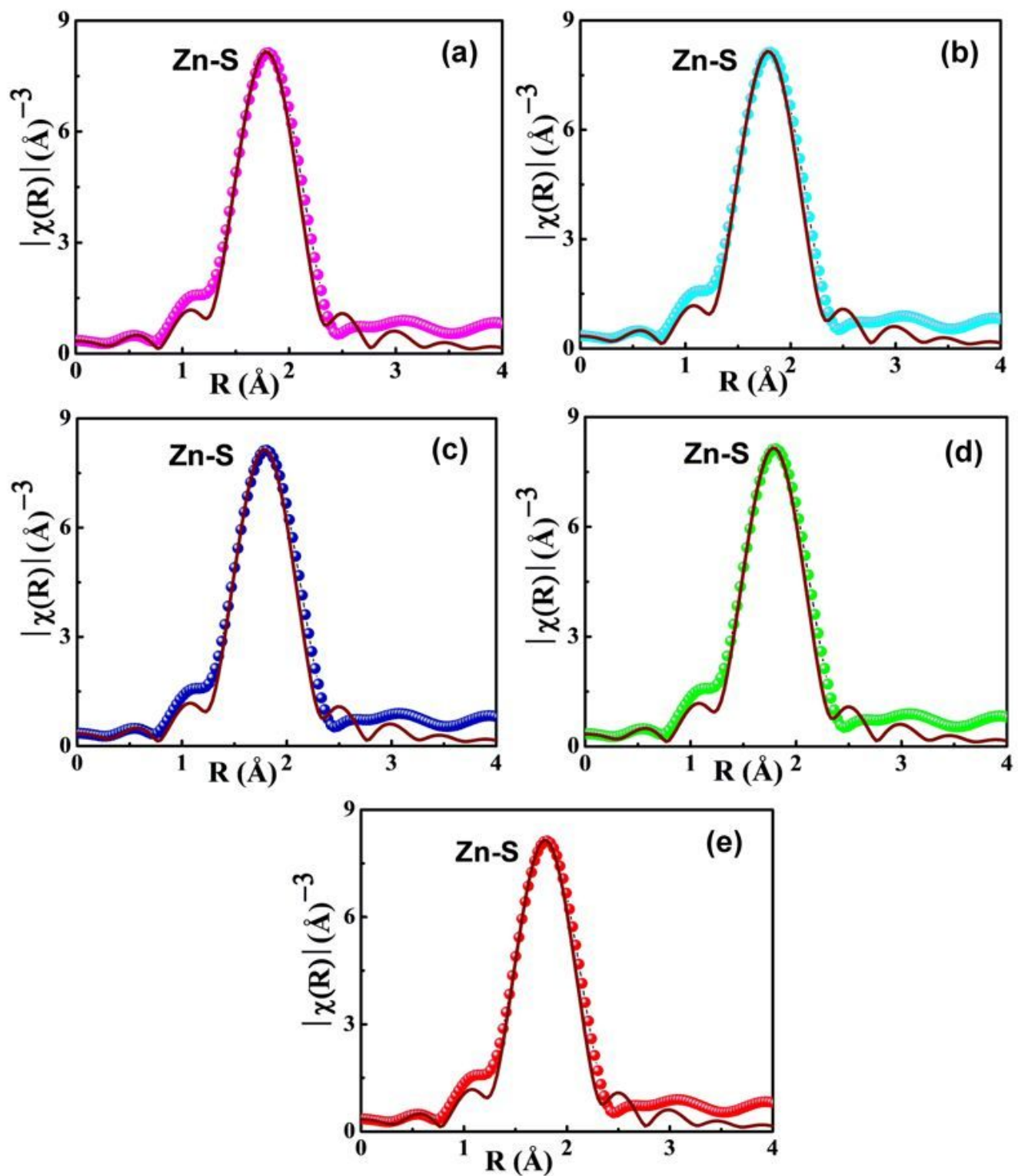


Figure 9

The best fitted experimental vs. data with theoretically created plot (showed in solid line) at Zn K-edge of (a) Ni₀, (b) Ni_{0.5}, (c) Ni₁, (d) Ni₂ and (e) Ni₄ nanocrystals

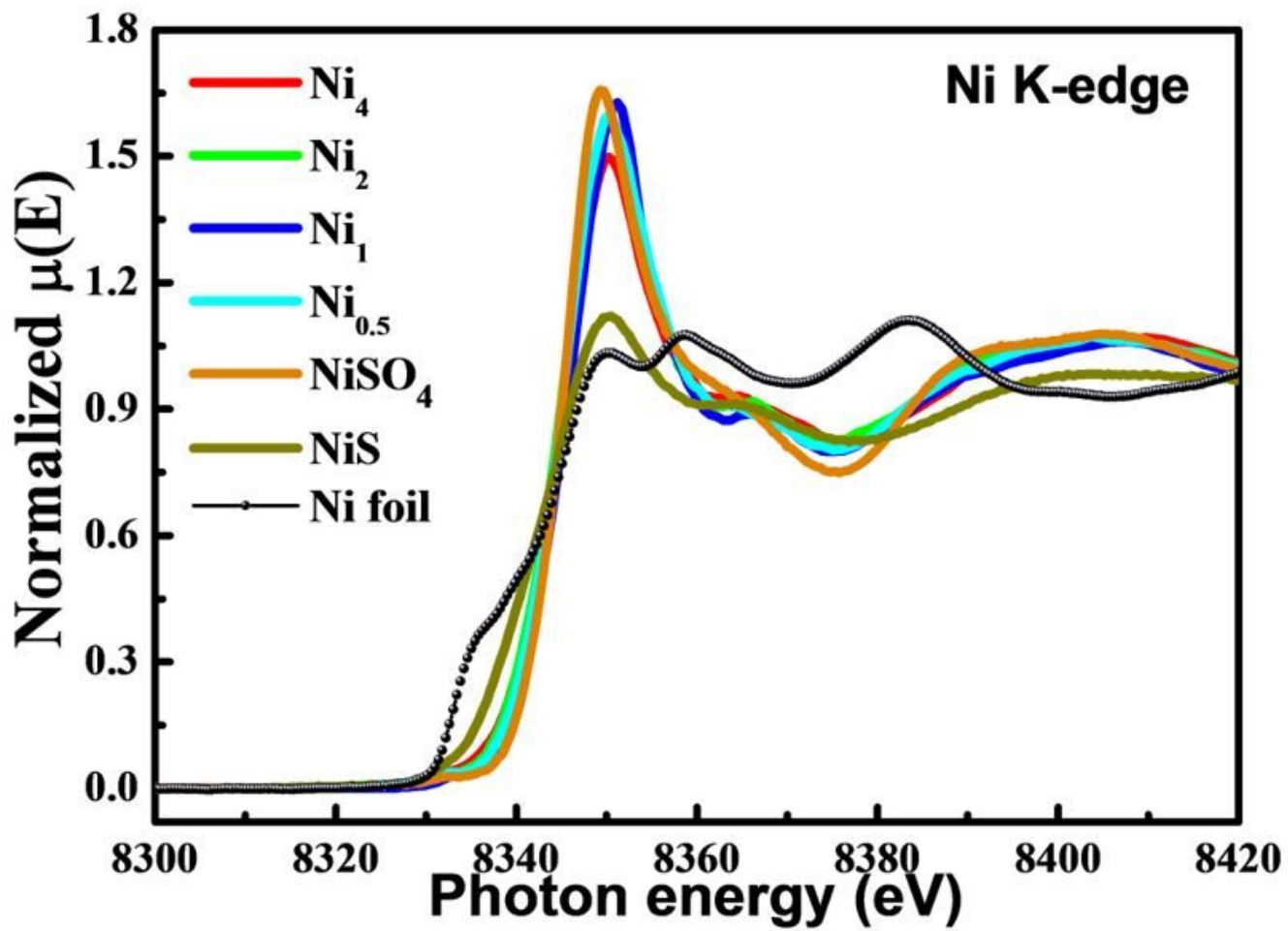


Figure 10

The normalized XANES data observed at Ni K-edge of the $\text{Zn}_{1-x}\text{Ni}_x\text{S}$ nanocrystals

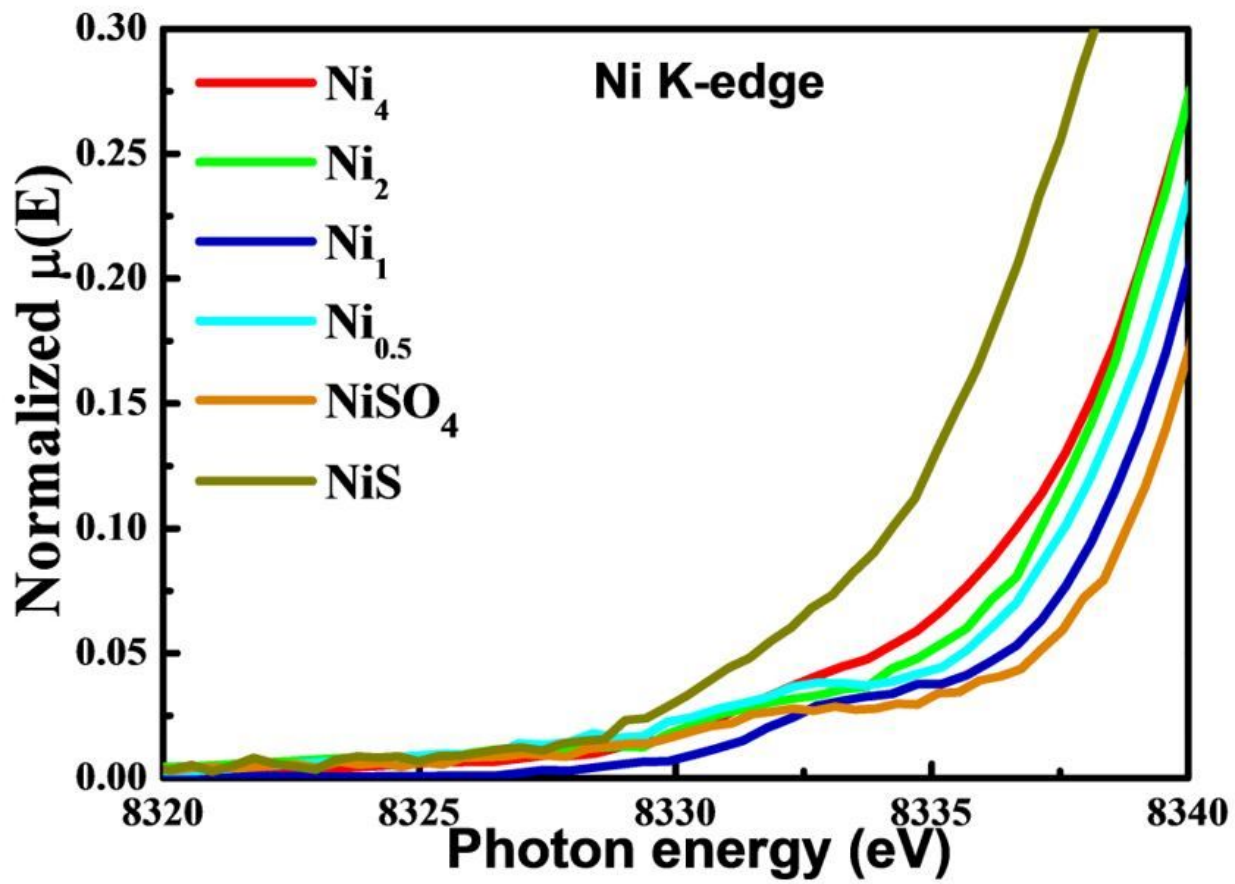


Figure 11

The pre-edge characteristic of the nickel doped ZnS NCs with reference to NiS and NiSO₄ samples at Ni K-edge

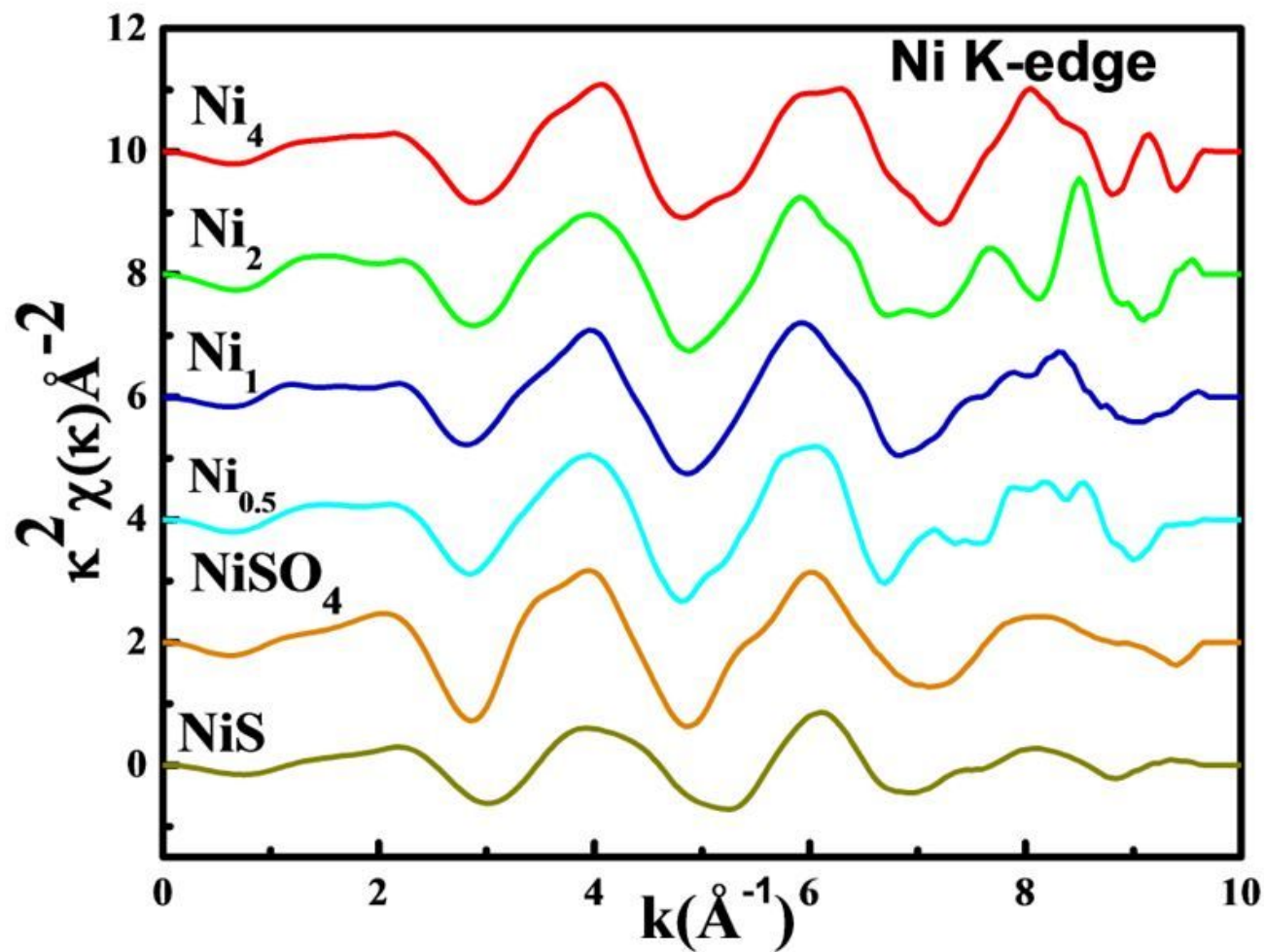


Figure 12

The K2 weighted X(k) spectra obtained at Ni K-edge of the $\text{Zn}_{1-x}\text{Ni}_x\text{S}$ nanocrystals

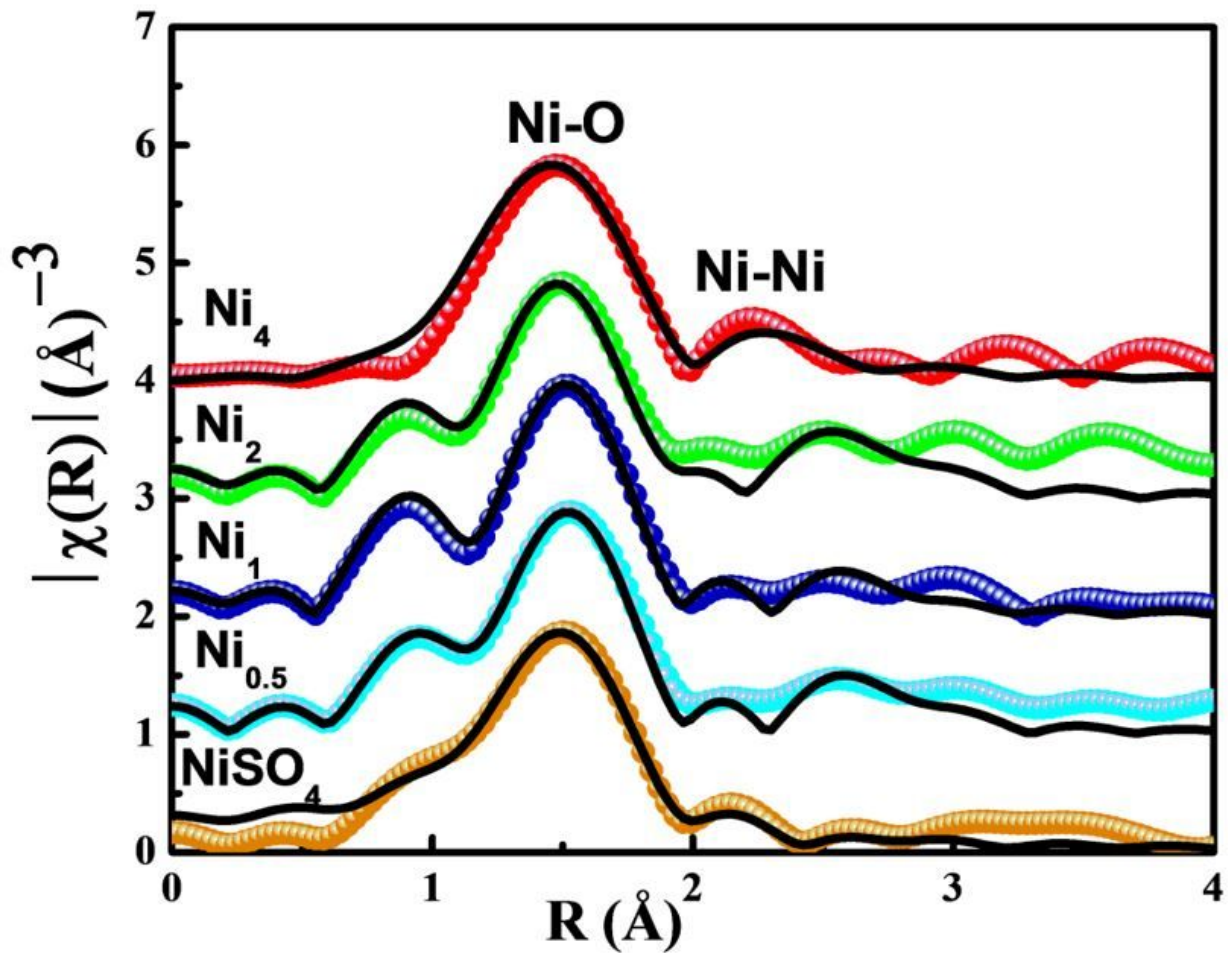


Figure 13

The best fitted experimental $X(R)$ vs. R data with theoretically created data (showed in solid line) at Ni K-edge of the $Zn_{1-x}Ni_xS$ nanocrystals

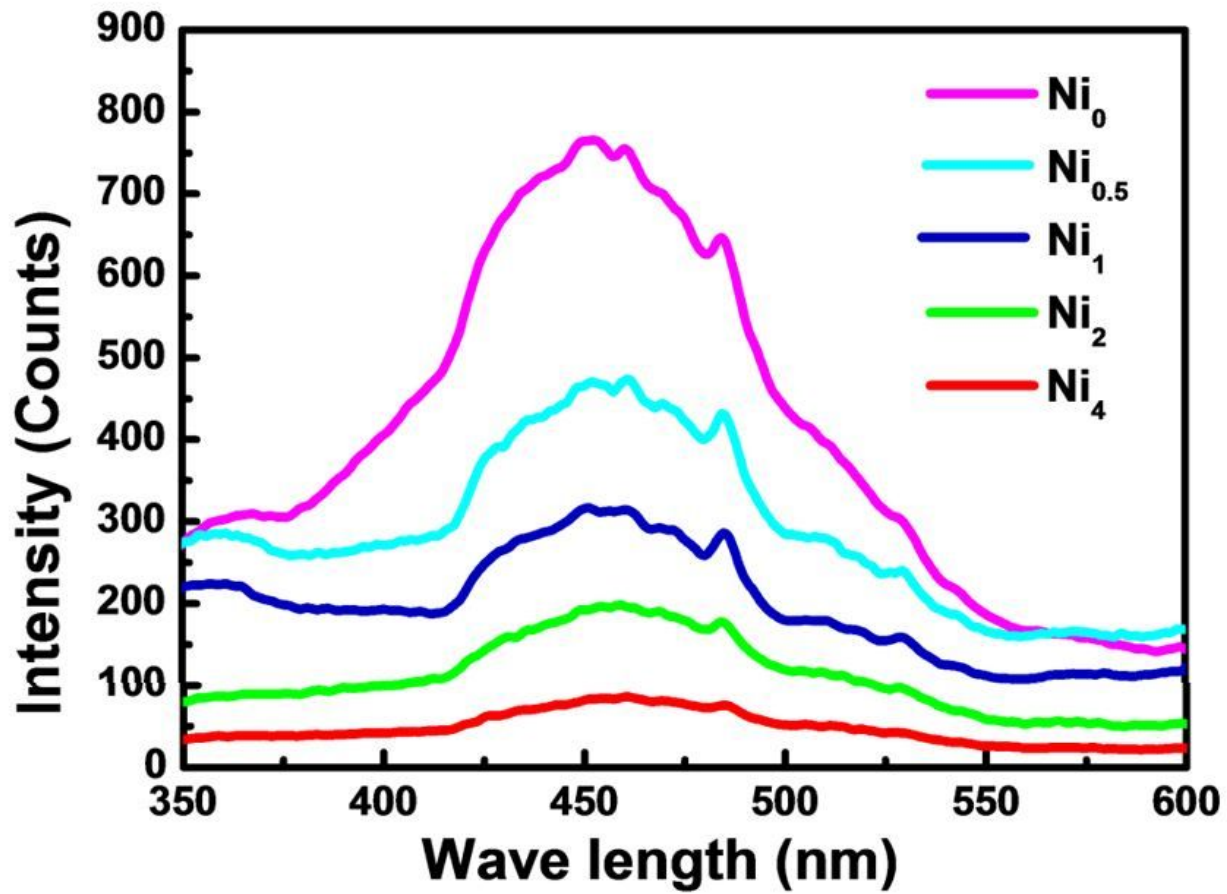


Figure 14

The photoluminescence spectrum of Zn_{1-x}Ni_xS ($0 \leq x \leq 0.04$) nanocrystals observed by exciting at 320 nm

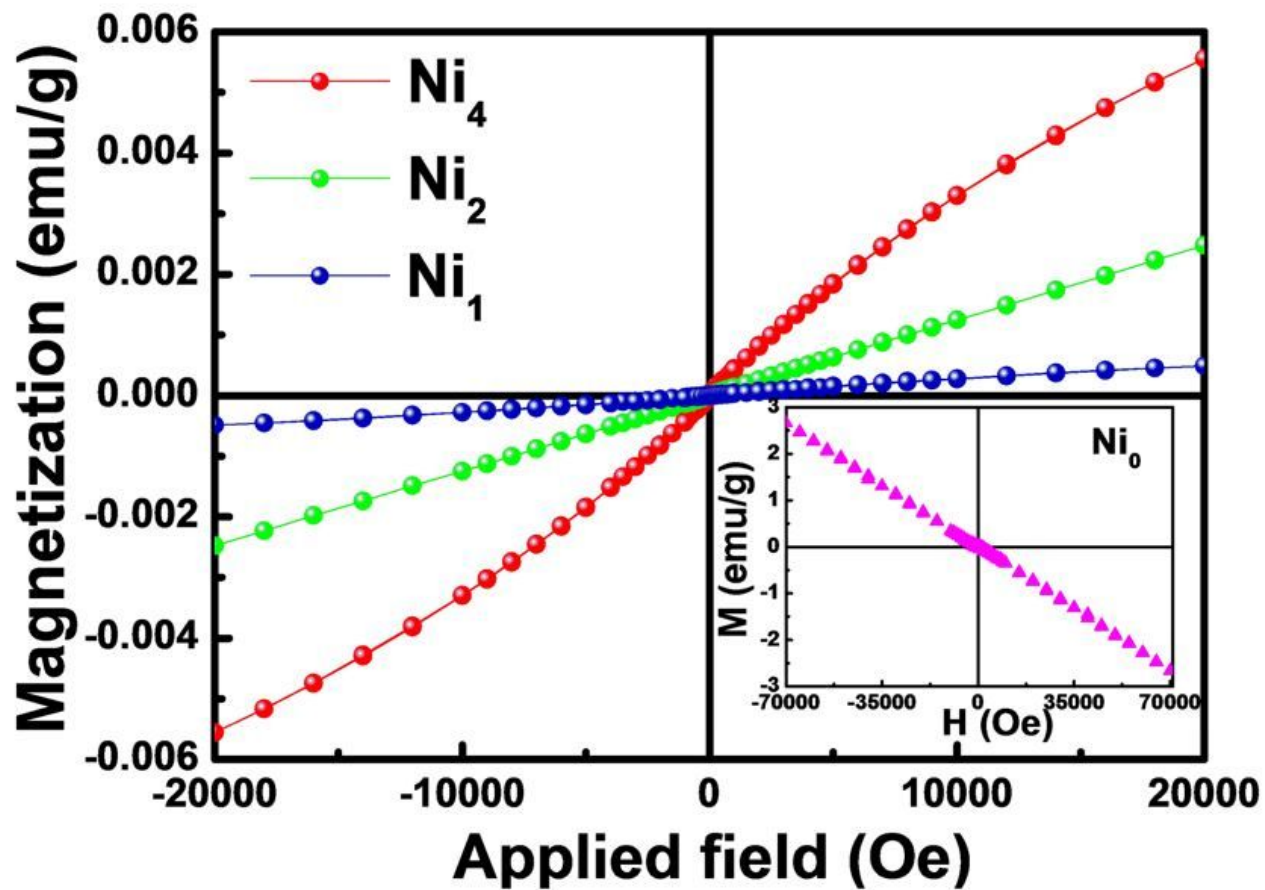


Figure 15

Magnetization vs. applied field measured in the range of ± 20000 Oe at 300 K of Ni₁, Ni₂, Ni₄ nanocrystals samples and the inset is the magnetization of Ni₀ nanocrystals observed in the range of ± 70000 Oe at 300 K

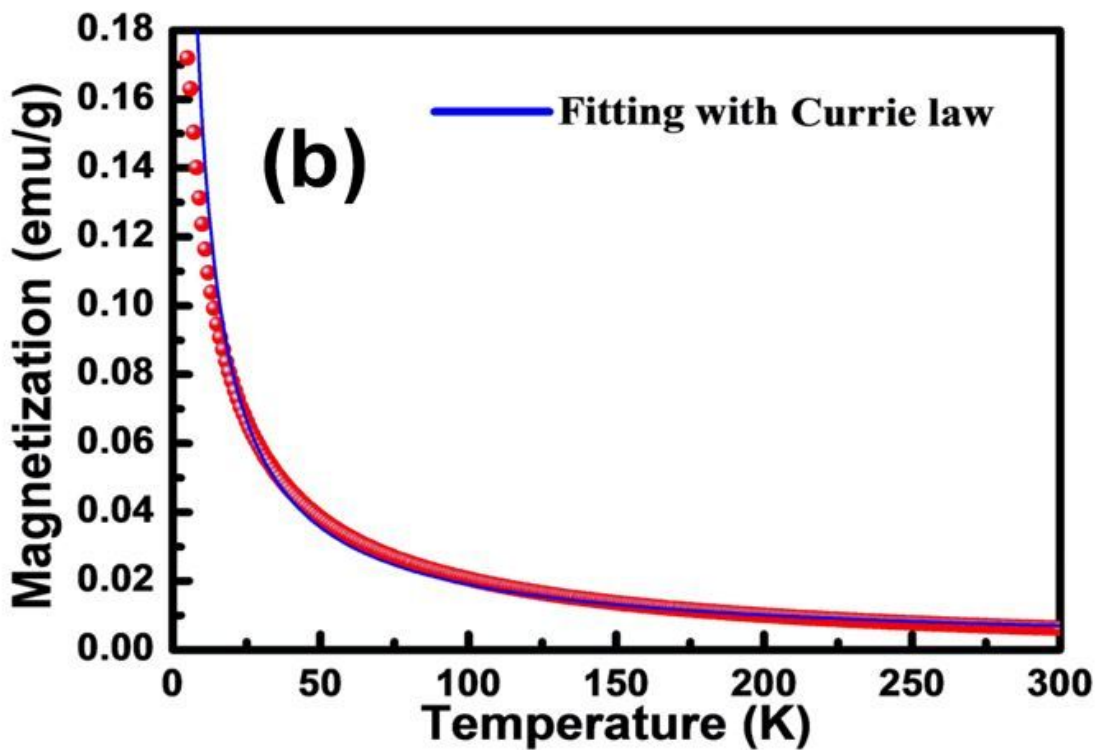
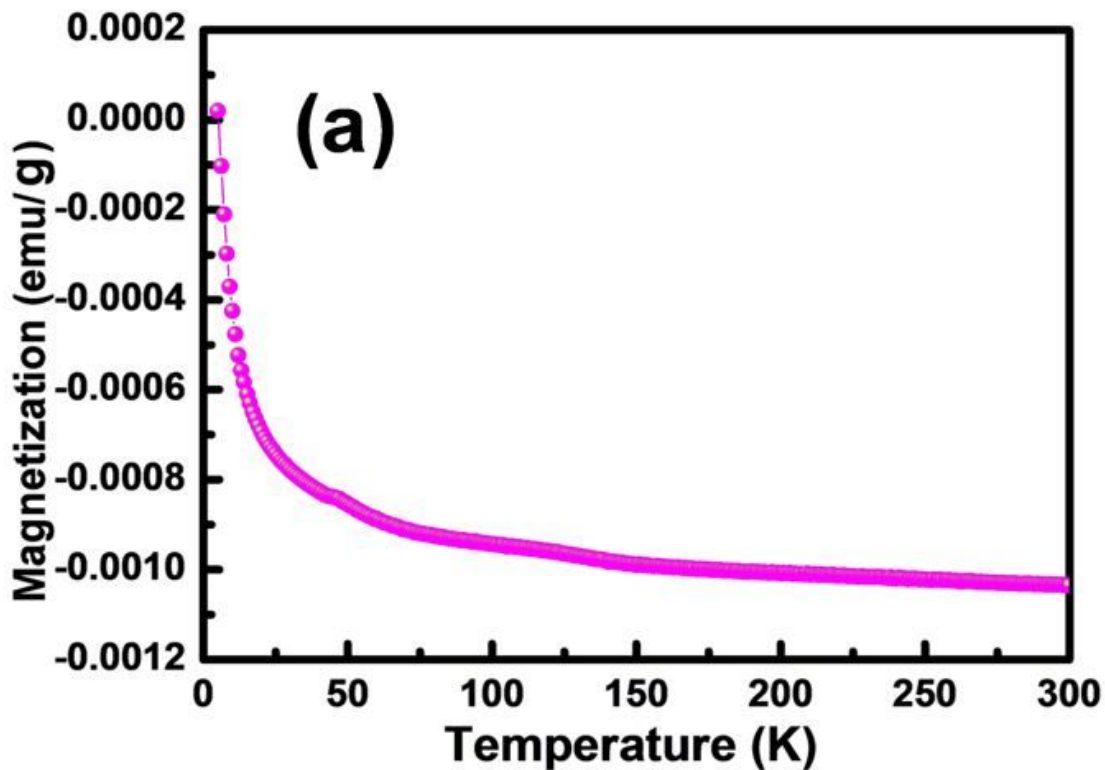


Figure 16

Magnetization vs. temperature plot of (a) Ni₀ nanocrystals and (b) Ni₄ nanocrystals (with fitting) at fixed field of 1000 Oe